

Near-Instantaneously Adaptive Learning-Assisted and Compressed Sensing-Aided Joint Multi-Dimensional Index Modulation

Xinyu Feng, *Student Member, IEEE*, Mohammed EL-Hajjar, *Senior Member, IEEE*, Chao Xu, *Senior Member, IEEE*, and Lajos Hanzo, *Life Fellow, IEEE*

Abstract—Index Modulation (IM) is capable of striking an attractive performance, throughput and complexity trade-off. The concept of Multi-dimensional IM (MIM) combines the benefits of IM in multiple dimensions, including the space and frequency dimensions. On the other hand, IM has also been combined with compressed sensing (CS) for attaining an improved throughput. In this paper, we propose Joint MIM (JMIM) that can utilize the time-, space- and frequency-dimensions in order to increase the IM mapping design flexibility. Explicitly, this is the first paper developing a jointly designed MIM architecture combined with CS. Three different JMIM mapping methods are proposed for a space- and frequency-domain aided JMIM system, which can attain different throughput and diversity gains. Then, we extend the proposed JMIM design to three dimensions by combining it with the time domain. Additionally, to circumvent the high detection complexity of the proposed CS-aided JMIM design, we propose Deep Learning (DL) based detection. Both Hard-Decision (HD) as well as Soft-Decision (SD) detection are conceived. Additionally, we investigate the adaptive design of the proposed CS-aided JMIM system, where a learning-based adaptive modulation configuration method is applied. Our simulation results demonstrate that the proposed CS-aided JMIM (CS-JMIM) is capable of outperforming its CS-aided separate-domain MIM counterpart. Furthermore, the learning-aided adaptive scheme is capable of increasing the throughput while maintaining the required error probability target.

Index Terms—Index Modulation (IM), Compressed Sensing-aided Multi-Dimensional Index Modulation (CS-MIM), Soft-Decision Detection, Machine Learning, Neural Network.

NOMENCLATURE

Acronym

Approx-Log-MAP Approximate Logarithm MAP
 AWGN Additive White Gaussian noise
 BER Bit-Error Ratio
 CE Channel Estimation
 CoE Cost Efficiency
 CP Cyclic Prefix
 CS Compressed Sensing
 CS-GFIM-CSM CS-aided Generalized SIM with SM
 CS-JMIM Compressed Sensing-aided JMIM
 CS-MIM CS-aided MIM

CS-STFIM CS-Aided Space-Time-Frequency Index Modulation 42
 CSI Channel State Information 43
 DL Deep Learning 44
 DM Dispersion Matrix 45
 DNN Deep Neural Network 46
 EE Energy Efficiency 47
 FC Fully-Connected 48
 FD Frequency Domain 49
 FFT Fast Fourier Transform 50
 GFIM Generalized Space-and-Frequency IM 51
 GSIM Generalized SIM 52
 HD Hard-Decision 53
 IFFT Inverse Fast Fourier Transform 54
 IM Index Modulation 55
 JIM Joint Index Mapping 56
 JMIM Joint Multi-dimensional Index Modulation 57
 KNN K -nearest Neighbour 58
 LLR Log-Likelihood Ratio 59
 MAP Maximum A Posteriori 60
 MIM Multi-dimensional Index Modulation 61
 MIMO Multiple-In and Multiple-Out 62
 ML Maximum Likelihood 63
 mmWave Millimeter Wave 64
 MSE Mean Square Error 65
 OFDM Orthogonal Frequency Division Multiplexing 66
 OFDM-IM OFDM with Index Modulation 67
 PSK Phase Shift Keying 68
 QAM Quadrature Amplitude Modulation 69
 QSF-IM Quadrature Space-Frequency IM 70
 QSM Quadrature SM 71
 RA Receive Antenna 72
 RD Real Domain 73
 Relu Rectified Linear Unit 74
 RF Radio Frequency 75
 RSC Recursive Systematic Convolutional 76
 SD Soft-Decision 77
 SE Spectral Efficiency 78
 SF Space-Frequency 79
 SFSK Space-Frequency Shift Keying 80
 SIM Subcarrier-Index Modulation 81
 SM Spatial Modulation <https://www.zhihu.com/tion> 82
 SNR Signal-to-Noise Ratio 83
 SpD Spatial Domain 84
 ST Space-Time 85
 86

The authors are with the School of Electronics and Computer Science, University of Southampton, Southampton SO17 1BJ, U.K. (e-mail: xf2u18,meh,cx1g08,lh@ecs.soton.ac.uk).

L. Hanzo would like to acknowledge the financial support of the Engineering and Physical Sciences Research Council projects EP/W016605/1 and EP/X01228X/1 as well as of the European Research Council's Advanced Fellow Grant QuantCom (Grant No. 789028)

87	STSK	Space-Time Shift Keying
88	TA	Transit Antenna
89	TD	Time Domain
90	TS	Time Slot
91	TSF	Time-Space-Frequency
92	VD	Virtual Domain
93	Symbols	
94	N_r	number of RAs
95	N_t	number of TAs
96	N_c	number of subcarrier for each frame
97	N_f	number of subcarrier per group in FD
98	N_{vt}	number of TAs in VD
99	N_v	number of subcarriers per group in VD
100	G	number of group
101	b	total bits number of each frame
102	b_g	bits number per group
103	K	number of activated index in JMIM matrix
104	Q	number of total realizations of JMIM mapping DMs
105	S	ST block
106	D_q	The q -th DM of Q total JIM DMs
107	D_i	Selected DM of Q total JIM DMs
108	χ	M-ary PSK or QAM constellation
109	x	Selected constellation symbol from χ
110	S_g	combined signal after JMIM and PSK/QAM
111	g_s	number of sub-groups in grouped JIM methods of JMIM
112		
113	gsx	number of split groups in virtual FD
114	gsy	number of split groups in virtual spatial domain
115	N_q	column length of coded JMIM DM
116	n_q	number of active subcarriers in each column of coded JMIM
117		
118	T	number of TS for transmitting in TD
119	T_v	number of TS for transmitting in VD
120	gsz	number of split groups in virtual TD
121	s	JMIM vector after block creator in VD
122	A	CS measurement matrix
123	$s^{(RD)}$	JMIM vector after CS
124	h_α	channel model in TD
125	H_α	channel model in FD
126	Y	Received signal
127	W	Additive White Gaussian noise
128	N_0	noise power of AWGN
129	$\bar{D}(\beta)$	all the possible realizations of the JMIM DM
130	W_n	weights of n -th neuron
131	\mathcal{X}	all the possible realizations of the selected PSK/QAM symbol
132		
133	θ_n	bias of n -th neuron
134	B	sample size of current iteration of DNN training phase
135	L_a	de-interleaved LLR sequence of L_e
136	L_e	output extrinsic LLR after soft demodulation
137	c	coded bit sequence of information bits
138	u	information bit sequence stream
139	$\mathcal{X}_{\gamma,\beta}$	the PSK/QAM symbol at the β -th CS-JMIM DM
140	\mathcal{X}_1^l	subset of the legitimate equivalent signal \mathcal{X} corresponding to bit $u_l = 1$
141		
142	\mathcal{X}_0^l	subset of the legitimate equivalent signal \mathcal{X} corresponding to bit $u_l = 0$
143		
144	ξ	the SNR value of a symbol with a BER lower than

		the target BER value for adaptive modulation	145
	\mathcal{T}	training sets of SNR with different the adaptive mode	146
	N_p	total number of instantaneous SNR values with BER under the target	147
			148

I. INTRODUCTION

INDEX Modulation (IM) [1] can be considered as an energy-efficient candidate for next-generation wireless systems as a benefit of its flexible resource activation [2]. The concept of IM has been derived from that of Spatial Modulation (SM), which is a low-complexity Multiple-In and Multiple-Out (MIMO) scheme capable of striking a flexible performance vs. complexity trade-off using a single Radio Frequency (RF) chain [2]–[4]. Then, the concept of SM has also been extended to the frequency and time dimensions, where the philosophy of IM has been proposed [5], [6]. In the Frequency Domain (FD), the IM combined with Orthogonal Frequency Division Multiplexing (OFDM) is referred to as Subcarrier-IM (SIM), where only a fraction of the subcarriers is activated for signal transmission and the index of active subcarriers conveys extra information bits [7]. The effective signal power of the subcarriers activated in the FD is amplified, without increasing the time domain signal power after Inverse Fast Fourier Transform (IFFT). This results in a higher Signal-to-Noise Ratio (SNR) for the modulated symbols without requiring extra radiated power. Then, Tsonev *et al.* [8] proposed an enhanced SIM and Basar *et al.* [9] conceived a novel IM-aided OFDM (OFDM-IM) scheme for increasing the spectral efficiency. However, subcarrier-index modulated OFDM suffers from significant throughput reduction compared to the classic OFDM due to the deactivation of a number of subcarriers. Hence, Zhang *et al.* [10] proposed an improved SIM concept relying on Compressed Sensing (CS) [11], which benefits from the sparsity of symbols in the FD by compressing the sparse transmit vector [12].

To further increase the overall performance, Datta *et al.* proposed the concept of Generalized SIM (GSIM) and proved that Generalized Space-and-Frequency IM (GSFIM) achieves better performance than MIMO-OFDM. Their solution conveyed extra information in the SM part compared to GSIM [13]. However, the detection complexity of GSFIM escalates. Hence, Chakrapani *et al.* [14] proposed a message passing based low-complexity detection method for reducing the complexity of GSFIM detection. Furthermore, inspired by the SM and Quadrature SM (QSM) concepts [15], Quadrature Space-Frequency IM (QSF-IM) was proposed in [16], which applies a twin-antenna constellation for the in-phase and quadrature-phase transmission, in order to increase the throughput without extra energy consumption. Hence this solution struck a compelling Spectral Efficiency (SE), Energy Efficiency (EE) and Cost Efficiency (CE) trade-off.

Furthermore, several researchers considered the design of Multi-Dimensional Index Modulation (MIM) relying on both the Spatial Domain (SpD) and FD. For example, Space-Frequency Shift Keying (SFSK) [17] relies on an SFSK Dispersion Matrix (DM), which achieves beneficial transmit diversity in rapidly time-varying channels. Space-Time Shift

TABLE I: Contrasting our contributions to the literature

Contribution	proposed*	[10]	[24]	[22]	[25]	[26]	[27]	[28]	[29]	[30]
Index modulation	✓	✓	✓	✓	✓	✓	✓	✓	✓	✓
CS at transmitter	✓	✓		✓						
Learning aided detector	✓		✓		✓			✓	✓	✓
Soft decision detector	✓		✓				✓		✓	
Adaptive design for index modulation	✓									✓
Multi-dimensional index modulation	✓			✓					✓	
Joint index mapping design	✓			✓					✓	
3-Dimensional joint index modulation	✓									

201 Keying (STSK) constitutes another multi-functional MIMO
 202 technique in the family of MIM. It combines the Time Domain
 203 (TD) and the SpD and it is capable of striking a beneficial
 204 diversity versus multiplexing trade-off [18]. More specifically,
 205 in STSK, Q DMs are designed for spreading the signal over
 206 T Time Slots (TSs) and M Transmit Antennas (TA) in the
 207 TD and the SpD, respectively. Furthermore, the IM design
 208 activates one out of the Q DMs for transmission, hence $\log_2 Q$
 209 extra IM bits may be conveyed. By appropriately adjusting
 210 these parameters, improved Bit Error Ratio (BER), throughput
 211 and complexity trade-offs may be struck [19].

212 Additionally, the concept of MIM was proposed in [20],
 213 which is capable of improving the degrees of freedom, hence
 214 achieving all the benefits of the IM concept in several domains
 215 without introducing extra deployment costs, such as extra RF
 216 chains or transmission power. Furthermore, Lu *et al.* [21]
 217 proposed Compressed-Sensing-Aided Space-Time Frequency
 218 Index Modulation (CS-STFIM) to combine CS techniques
 219 with STSK and OFDM-IM, which is an MIM system concept
 220 that inherits the benefits of both STSK and OFDM-IM. As a
 221 further advance, SM was also integrated into this MIM scheme
 222 for TA selection in [22]. In [6], the concept of multi-functional
 223 layered SM was proposed, which offers flexible trade-offs in
 224 terms of performance, hardware cost and power dissipation.

225 However, in previous MIM schemes, the index selection
 226 was performed separately in each dimension. By contrast, in
 227 this paper, we extend this concept to a Joint MIM system,
 228 where we jointly designs the IM in several dimensions. More
 229 specifically, the degrees of freedom of the IM mapping design
 230 is increased by harnessing multiple dimensions, which leads
 231 to a more flexible trade-off between the throughput, power
 232 efficiency, and cost. In this case, both SFSK and STSK can be
 233 considered as special cases of the proposed joint MIM (JMIM)
 234 family. JMIM may also be combined with CS techniques for
 235 increasing the spectral efficiency.

236 However, the joint detection of multiple dimensions leads
 237 to massive computational complexity at the receiver side.
 238 More specifically, conventional Maximum Likelihood (ML)
 239 detection, suffers from a rapidly escalating complexity upon
 240 increasing in the number of dimensions [31]. Coherent detec-
 241 tion also requires the accurate knowledge of Channel State
 242 Information (CSI) at the receiver side, which leads to a
 243 substantial pilot overhead [32] as well as to a high Channel
 244 Estimation (CE) complexity [33], [34]. In [22], CS-aided MIM
 245 (CS-MIM) was presented, where multiple detection stages
 246 were required for recovering the data from the constituent
 247 CS, STSK, OFDM-IM and SM schemes. As a result, near-

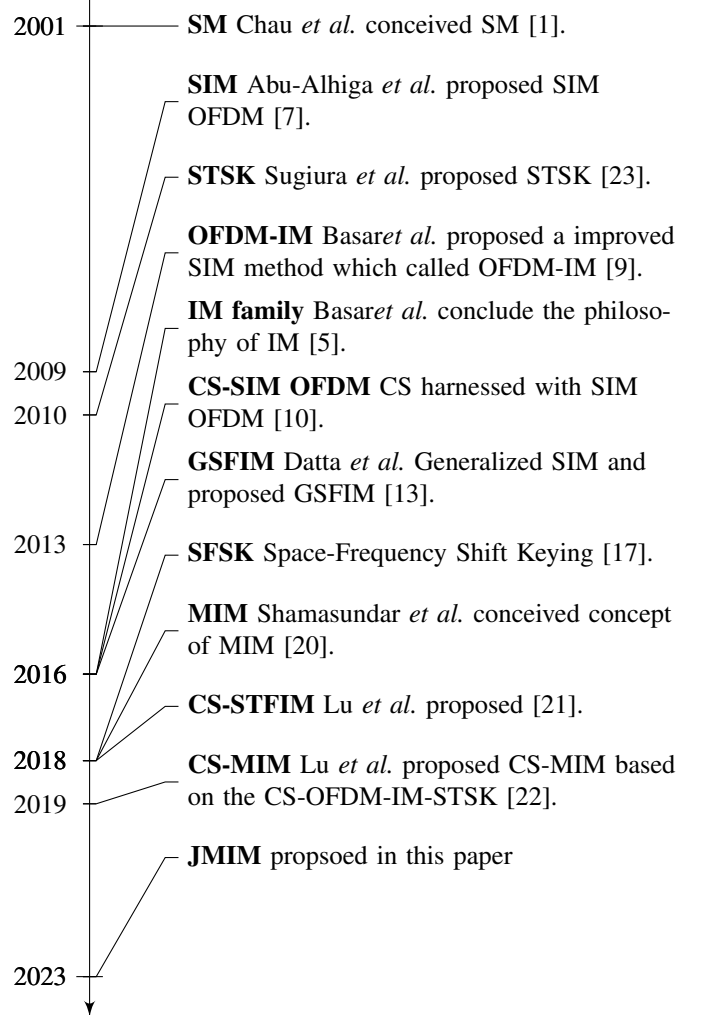


Fig. 1: Milestones of the index modulation family from single dimensional index modulation to MIM.

248 capacity operation can only be achieved, when Soft-Decision
 249 (SD) detection is used [35], but again, the complexity of MIM
 250 detection escalates with the number of IM dimensions.

251 Recently, learning-based detection has been used as an effi-
 252 cient tool for reducing the complexity of detection, while dis-
 253 pensing with the requirement of explicit CSI estimation [36].
 254 In [37], a Deep Neural Network (DNN) based model is
 255 proposed for detecting the OFDM-IM signal, while the authors
 256 of [38] and [39] harnessed convolutional neural networks
 257 for IM detection, when the CSI is available at the input of
 258 the detector. By contrast, blind learning based detection was

designed for Millimeter Wave (mmWave) IM in [28] and for multi-set STSK in [29]. However, the authors of [29] only investigated the combination of basic SD and Deep Learning (DL). In [36], both DNN-based Hard-Decision (HD) and iterative SD assisted blind detection have been proposed for CS-MIM.

Additionally, given the flexibility of our CS-aided JMIM (CS-JMIM) design, we can adapt the JMIM mapping to hostile time-varying channel environments to improve the attainable performance. Hence, the concept of adaptive modulation can be intrinsically amalgamated with CS-JMIM to improve the attainable throughput, while maintaining a specific target BER. Yang *et al.* proposed machine learning aided adaptive SM [40], while Liu *et al.* [41] conceived learning-assisted IM for mmWave communications. In their follow-on research, they further developed the work by considering CE employing sparse Bayesian learning for accurate CSI estimation [42].

Table I boldly contrasts the novelty of this paper to the literature. More explicitly, the contributions of this paper can be further detailed as follows:

- 1) We propose the CS-JMIM system concept and present several JMIM mapping matrix designs. Then, we demonstrate that the proposed JMIM mapping design is capable of striking an attractive trade-off between diversity and throughput.
- 2) We propose a DL-based HD detection aided CS-JMIM system that can achieve near-ML performance, while imposing significantly reduced complexity. Furthermore, we propose a DNN-aided SD detector for the proposed CS-JMIM that is capable of achieving near-capacity performance.
- 3) Both a K -nearest neighbour (KNN) algorithm based and a DL-assisted adaptive modulation scheme is proposed for CS-JMIM. We demonstrate that the learning-assisted adaptive CS-JMIM scheme is capable of selecting more appropriate CS-JMIM mapping design for transmission than its conventional threshold-based adaptive counterparts. Hence it can obtain a significant throughput gain over the conventional threshold-based adaptive method.
- 4) Our simulation results demonstrate that the proposed learning-based detector is capable of approaching the performance of the conventional coherent detection techniques at a reduced detection complexity. We also provide the associated capacity and throughput analysis, for characterising the trade-off between each mapping matrix and the benefits of the learning-assisted adaptive method.

The rest of the paper is organized as follows. In Section II, the system model of CS-JMIM is presented. In Section III, we characterize both HD and SD based learning-aided detectors. Then, in Section IV we present our proposed adaptive system design. In Section V, we present our simulation results, while our conclusions are offered in Section VI.

II. SYSTEM MODEL

In this section, we introduce the transceiver model of the proposed CS-JMIM system employing N_t TAs and N_r Receive Antennas (RAs). Fig. 2 shows the block diagram of the

CS-JMIM system considered, where b bits are equally divided into G groups. We consider OFDM having N_c subcarriers, which are then split into G groups and each group has $N_f = N_c/G$ subcarriers in the FD¹, while N_{vt} TAs and N_v subcarriers of each group are applied for the CS-JMIM system in the Virtual Domain (VD)². To be more specific, in each subcarrier group, there are N_v available subcarrier indices within the VD, where the dimension N_v of the VD is larger than the dimension N_f of the FD. Similarly, N_{vt} antennas in the VD are larger than the N_t antennas of the SpD. For each group of b bits as $b_g (g = 1, 2, \dots, G)$, b_g^1 bits are used for generating K Phase Shift Keying/Quadrature Amplitude Modulation PSK/QAM symbols, while the remaining b_g^2 bits are mapped to the JMIM mapping matrix selector, which chooses a specific mapping matrix out of Q JMIM matrices. Then, these K PSK/QAM codewords and the selected JMIM mapping DM are combined to generate a Space-Time (ST) block \mathcal{S} . Afterwards, the block creator of Fig. 2 collects all codewords from the G groups for forming a frame, which is mapped to multiple index domains by the carrier index mapper, followed by the CS method and OFDM modulation, as shown in Fig. 2. Then, after transmission over the wireless channel, the receiver estimates the channel and detects the signal. At the receiver side, the signal is transformed back to the subcarrier symbols and each JMIM group signal is detected separately.

In the following, we present the details of the processing stages at the transmitter and the receiver. In this case, we only focus our attention on a single group instead of G groups, since the same procedure is applied to all groups, as shown in Fig.2. The transmitter model is introduced in Section II-A, followed by the receiver model in Section II-B.

A. Transmitter

As shown in Fig. 2, b bits are split into G groups, where the b_g bits, ($g = 1, 2, 3 \dots G$) of each group are split into two parts by the block splitter: b_g^1 bits are used for JMIM mapping matrix selection and b_g^2 bits for the classic PSK/QAM. In the following we explain in detail the Joint Index Mapping (JIM) part of the CS-JMIM transmitter of Fig. 2.

1) *Joint Index Mapping*: As shown in Fig.2, the N_c subcarriers of the OFDM symbol are divided into G groups of size N_f , with $N_f = N_c/G$. For each b_g group of bits, the first part b_g^1 is used for selecting the active DM from the Q candidates $\mathcal{D}_1, \mathcal{D}_2, \dots, \mathcal{D}_q, \dots, \mathcal{D}_Q$ with $\mathcal{D}_q \in \mathbb{C}^{N_v \times N_{vt}}$, $q = 1, 2, \dots, Q$. The second part is used for determining the constellation symbol, which is employed for modulating the active DM. The classic constellation symbol is then selected from a M -ary PSK or QAM constellation \mathcal{X} .

Let us denote the selected DM and the selected constellation symbol, respectively, by $\mathcal{D}_i, i \in \{1, \dots, Q\}$ and $x, x \in \mathcal{X}$. Then the combined signal in group g can be expressed by

$$\mathcal{S}_g = x\mathcal{D}_i, g = 1, \dots, G. \quad (1)$$

In the following, we introduce three designs of the DMs. Firstly, to leverage the multi-dimensionality of MIM systems,

¹FD is the OFDM symbol domain after CS processing, as shown in Fig. 2.

²VD is the actual domain. This concept was firstly introduced in [10] to illustrate the CS techniques in IM systems to improve the spectral efficiency.

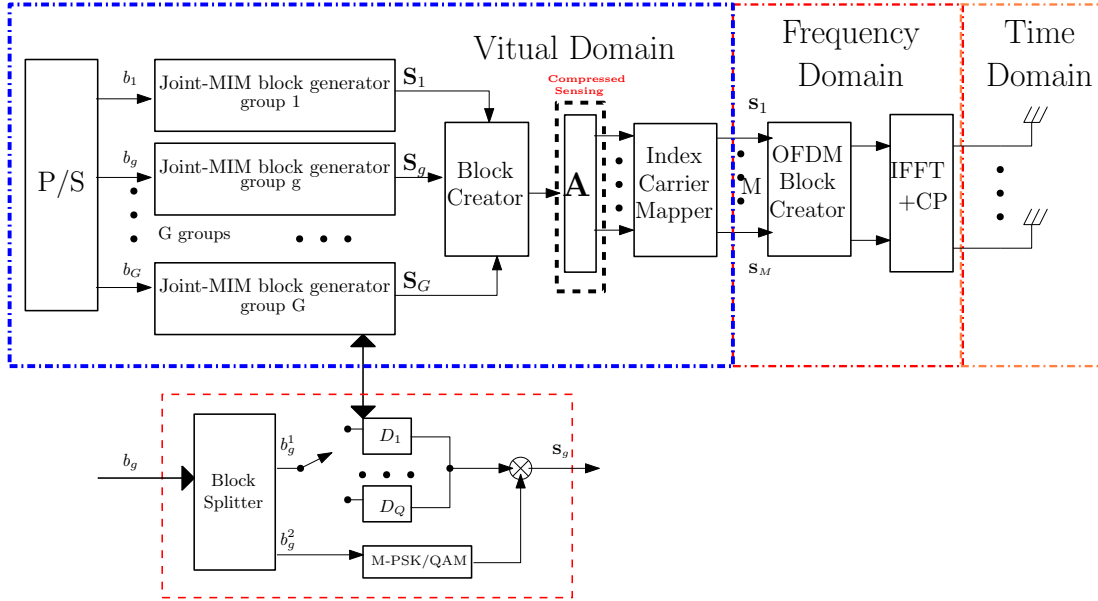


Fig. 2: CS-JMIM system transmitter block diagram.

368 the design of IM encompasses all dimensions. Then, the
 369 activation of the corresponding indices is guided by the
 370 coordinates of these joint dimensions, which is detailed in the
 371 following section in the context of a DM design referred to
 372 as General JIM. Secondly, to strike a design trade-off between
 373 the throughput and diversity gain attained, we can further split
 374 the joint multi-dimensional matrix into sub-group matrices,
 375 where different general JIM DMs can be selected for each
 376 sub-group matrix. We refer to this mapping design as Grouped
 377 JIM, which is further detailed in the following sections.
 378 Additionally, we introduce a coded DM design for achieving
 379 a high diversity gain, which is detailed in the following
 380 sections. Furthermore, we start a discussion considering the
 381 Space-Frequency (SF) dimensions and then we present a 3-
 382 dimensional mapping design for the Time-Space-Frequency
 383 (TSF) dimensions of JMIM.

384 *a) General Joint Index Mapping:* As JIM, first we con-
 385 sider joint SF DM design. The index is selected based on
 386 both dimensions' coordinates. We assign N_{vt} TAs and N_v
 387 subcarriers to a specific group, which results in $N_{vt}N_v$ possi-
 388 ble active positions and to a total of $C(N_tN_{vt}, K)$ legitimate
 389 realizations. As an example, let us consider having $K = 2$
 390 active subcarriers and $N_{vt} = 2, N_v = 2$ for each group. Then,
 391 we have $b_g^1 = \lceil \log_2 C(N_{vt}N_v, K) \rceil = \lceil \log_2 C(4, 2) \rceil = 2$ bits
 392 for selecting $K = 2$ active subcarriers out of 4 available
 393 subcarriers in each group, since we have $2^2 = 4$ legitimate
 394 combinations which equivalent to $Q = 4$ DMs, as shown in
 395 Table II. Fig.3 shows a block diagram of the general JIM
 396 example presented in Table II, where the activated index is
 397 then combined with the QAM symbol by the multiplier to
 398 form the combined symbol S . Furthermore, when compared
 399 to the CS-aided separate MIM system, CS-JMIM can attain
 400 comparable throughput as CS-MIM with significant sparsity.

401 *b) Grouped Joint Index Mapping:* Given a substantial
 402 number of TAs, subcarriers, and a limited quantity of active
 403 index elements K in each group, most elements in the DM

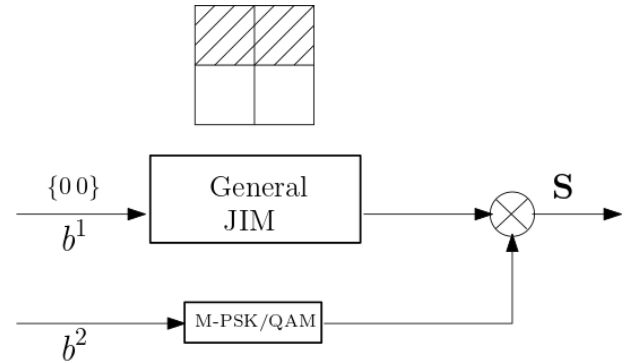


Fig. 3: Block diagram of the general JIM example in Table II with $b_1 = [0 \ 0]$.

TABLE II: An example selection procedure of joint SF index selection in a CS-JMIM system having $K = 2, N_v = N_{vt} = 2$

b_2	matrix No.	Indices	Allocation
[00]	D_1	(1, 2)	$\begin{bmatrix} 1 & 1 \\ 0 & 0 \end{bmatrix}$
[01]	D_2	(1, 3)	$\begin{bmatrix} 1 & 0 \\ 1 & 0 \end{bmatrix}$
[10]	D_3	(1, 4)	$\begin{bmatrix} 1 & 0 \\ 0 & 1 \end{bmatrix}$
[11]	D_4	(2, 3)	$\begin{bmatrix} 0 & 1 \\ 1 & 0 \end{bmatrix}$

404 remain inactive, leading to diminished SE. To address this, 404
 405 we propose grouped JIM, which divides the DM matrix into 405
 406 smaller sub-group matrices, each adopting a general JIM. Fur- 406
 407 thermore, striking a trade-off between throughput and diversity 407
 408 involves choosing either the same or different DMs across 408
 409 groups. To elaborate further, applying the same DM across 409
 410 all groups results in multiple copies of the information bits, 410
 411 which produces a diversity gain. On the other hand, employing 411
 412 different DMs for each group improve the throughput. 412

413 For example upon assuming $N_{vt} = 4, N_v = 4$ and $K = 2$
 414 for each groups DM results in $\mathbf{D}_q \in \mathbb{C}^{N_{vt} \times N_v}$. Then, we
 415 further split \mathbf{D}_q into four equal sub-matrices expressed as

$$\mathbf{D}_q = \begin{bmatrix} \mathbf{D}_q^{1,1} & \mathbf{D}_q^{2,1} \\ \mathbf{D}_q^{1,2} & \mathbf{D}_q^{2,2} \end{bmatrix}, \quad (2)$$

416 where we have $\mathbf{D}_q^i \in \mathbb{C}^{N_{vt}/2 \times N_v/2}, i = 1, 2, 3, 4$. For each
 417 sub-matrix $\mathbf{D}_q^{i,j}, (i = 1, 2, 3 \dots gsx), (j = 1, 2, 3 \dots gsy)$ general
 418 JIM can be applied. Here, gsx and gsy represent the number
 419 of sub-group's in the FD and SpD, respectively. In the above
 420 example, we can have a total of $gs = gsx \times gsy = 4$
 421 sub-groups and $b_g^1 = \lceil \log_2 C(4, 2) \rceil = 2$ bits for each sub-
 422 groups matrix. To maximize the throughput, four different
 423 sub-matrices can be aggregated to one DM \mathbf{D}_q to obtain 8
 424 bits in total. Fig.4 shows the block diagram of the grouped
 425 JIM, where we have four sub-groups of smaller general JIMM
 426 matrix. For a small general JIMM matrix we can apply $Q = 4$
 427 DMs in total, where we can assign 4×2 bits for all sub-groups.
 428 On the other hand, if four repeated sub-matrices are used, we
 429 can achieve similar structure of coded JIMM which will be
 430 discussed below.

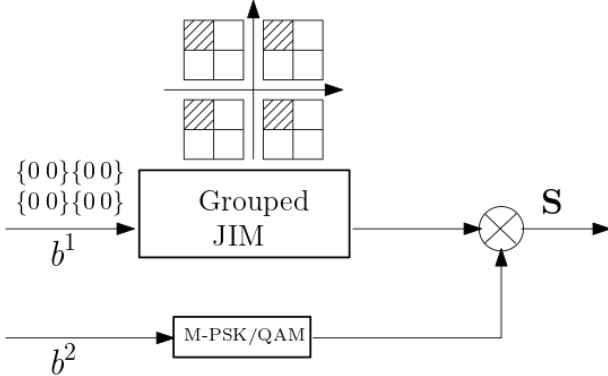


Fig. 4: Block diagram of a grouped JIM example with $b_1 = [0 0 0 0 0 0 0 0]$

431 *Subsequently, the grouped JIM optimally utilizes the avail-*
 432 *able space of the VD matrix, albeit at the expense of sparsity.*
 433 *By adjusting the index mapping of each sub-group, it offers*
 434 *significant throughput or diversity gains. However, this leads*
 435 *to a substantial increase in detection complexity for conven-*
 436 *tional methods, such as the ML detector.*

437 *c) Coded Joint Index Mapping:* Another way of further
 438 increasing the transmit diversity is to employ coded index
 439 mapping, where we use a circular shift based design of the
 440 DMs, which was proposed for SFSK in [17]. In this method,
 441 the number of active subcarriers in each column is n_q , with
 442 $N_q - n_q$ inactive subcarriers, where N_q is the column length
 443 of \mathbf{D}_q . Then, the second column is the circular down shift of
 444 the first column by one position. Similarly, other columns can
 445 be obtained based on the previous column distribution.

446 To elaborate a little further, using a 'toy' example, for $N_q =$
 447 $N_{vt} = 4, n_q = 2$, we can have $Q = C(N_q, n_q) = 6$ possible
 448 combinations, yielding $b_g^1 = \lceil \log_2 C(N_q, n_q) \rceil = 2$ bits. The

following is an example of a circular shifting based DM:

$$\begin{aligned} \mathbf{D}_1 &= \begin{bmatrix} 1 & 0 & 0 & 1 \\ 1 & 1 & 0 & 0 \\ 0 & 1 & 1 & 0 \\ 0 & 0 & 1 & 1 \end{bmatrix}, \mathbf{D}_2 = \begin{bmatrix} 1 & 0 & 1 & 0 \\ 0 & 1 & 0 & 1 \\ 1 & 0 & 1 & 0 \\ 0 & 1 & 0 & 1 \end{bmatrix}, \\ \mathbf{D}_3 &= \begin{bmatrix} 1 & 1 & 0 & 0 \\ 0 & 1 & 1 & 0 \\ 0 & 0 & 1 & 1 \\ 1 & 0 & 0 & 1 \end{bmatrix}, \mathbf{D}_4 = \begin{bmatrix} 0 & 0 & 1 & 1 \\ 1 & 0 & 0 & 1 \\ 1 & 1 & 0 & 0 \\ 0 & 1 & 1 & 0 \end{bmatrix}, \\ \mathbf{D}_5 &= \begin{bmatrix} 0 & 1 & 0 & 1 \\ 1 & 0 & 1 & 0 \\ 0 & 1 & 0 & 1 \\ 1 & 0 & 1 & 0 \end{bmatrix}, \mathbf{D}_6 = \begin{bmatrix} 0 & 1 & 1 & 0 \\ 0 & 0 & 1 & 1 \\ 1 & 0 & 0 & 1 \\ 1 & 1 & 0 & 0 \end{bmatrix}. \end{aligned}$$

Given $b_g^1 = 2$ bits, then $2^2 = 4$ DMs are selected for the CS-JMIM system.

Fig.5 shows a block diagram of the coded JIM, where we can apply the first JIM DM for $b_1 = [0 0]$ based on the code book used. *In this scenario, coded JIM offers the maximum diversity in the design of coded DMs, enabling reliable detection even in highly noisy environments.*

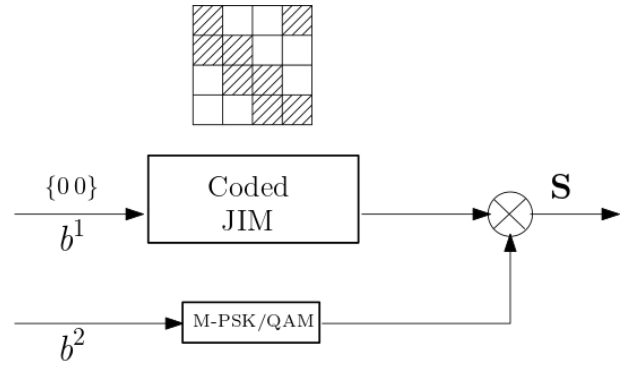


Fig. 5: Block diagram of a coded JIM example with $b_1 = [0 0]$

457 *d) 3-Dimensional Dispersion Matrix Design:* In this design,
 458 the TD is introduced as an extra dimension for the JIM.
 459 We assume that T_v TSSs are applied in the VD and T TSSs are
 460 used in the TD, while we have $T_v > T$. Then, we can assign
 461 three-dimensional DMs $\mathbf{D}_q \in \mathbb{C}^{N_v \times N_{vt} \times T_v}$. In this case, the
 462 above-mentioned three mapping techniques can be applied.

463 Specifically, for the general JIM we may consider the
 464 following example for further illustration. Let $K = 1$ and
 465 $N_{vt} = N_v = T_v = 2$ as shown in Fig. 6(a) and $b_g^1 = [001]$.
 466 More specifically, the three-dimensional matrix can be expressed
 467 in the coordinate form of (n_v, n_{vt}, t_v) . In this case,
 468 given the IM bits $b_g^1 = [010]$, we activate the fourth element in
 469 a set of 8 elements in this three-dimensional matrix with the
 470 coordinates $(2, 2, 1)$ as shown in Fig. 6(a). Then, the number
 471 of bits of this JMIM applied for the DM selection becomes
 472 $b_g^1 = \lceil \log_2 C(N_{vt} N_v T_v, K) \rceil = \lceil \log_2 C(8, 1) \rceil = 3$ bits.

473 Fig. 6(b) shows the structure of the grouped JIM applied in
 474 three dimensions. Similar to the SF matrix, the TSF matrix can
 475 be split into several equal sub-groups. As shown in Fig. 6(b),
 476 we assume $N_{vt} = N_v = T_v = 4$ and $K = 1$ for each group's
 477 DM, which results in $\mathbf{D}_q \in \mathbb{C}^{N_v \times N_{vt} \times T_v}$. Then, we further
 478 split \mathbf{D}_q into 8 equal sub-matrices. Each sub-group DM can

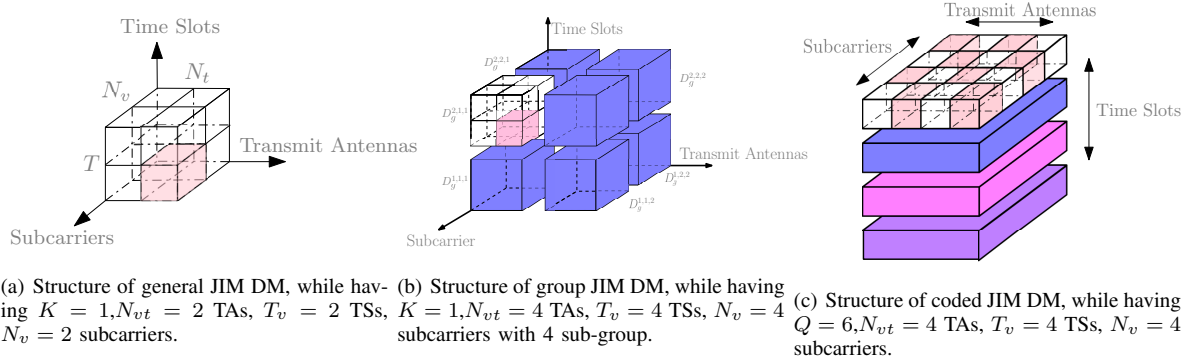


Fig. 6: Illustration of the structure for JIM DM in time-space-frequency domain

479 be expressed in the form of $D_g^{gsx,gsy,gsz}$, where gsx,gsy,gsz
 480 represents the split size in the FD, the SpD and the TD,
 481 respectively. For each sub-matrix $D_g^{gsx,gsy,gsz}$, general JIM
 482 can be applied within a set of $gs = gsx \times gsy \times gsz = 8$ sub-
 483 group matrices. Then, we can have $\lfloor \log_2 C(8,1) \rfloor = 3$ bits
 484 for each sub-matrix. To maximize the throughput, we can also
 485 assign different information to each sub-group and then the 8
 486 sub-matrices can be aggregated to form a single DM D_q
 487 to obtain $b_g^1 = gs \lfloor \log_2 C((N_v/gsx)(N_t/gsy)(T/gsz), K) \rfloor =$
 488 $8 \lfloor \log_2 C(8,1) \rfloor = 24$ bits for the JMIM design. Compared
 489 to the same DM size used in the general JIM, which has
 490 $b_g^1 = \lfloor \log_2 C(64,1) \rfloor = 6$ bits, the grouped JIM can provide a
 491 significant gain in the spectral efficiency. On the other hand,
 492 in order to attain a diversity gain, the sub-matrices can achieve
 493 maximum diversity gain, when all 8 sub-groups have the same
 494 active index.

495 Furthermore, for the coded JIM matrix design in three
 496 dimensions, the same method is applied for the first TS of
 497 the space-frequency matrix. Then, circular shifting is applied
 498 to the entire SF matrix to generate the next TS matrix
 499 with shifting by one position. As shown in Fig. 6(c), upon
 500 assuming $N_{vt} = N_v = T_v = 4$ for the DM size, as well as
 501 $N_q = n_q = 2$ for the activated subcarriers and $b^1 = [01]$, then
 502 the corresponding circular shifting based DM D_2 presented in
 503 the previous section is applied to the first TS of the 3D matrix.
 504 Then, we can generate each TS index mapping with the aid
 505 of a single position shifting, which can be represented as:

$$D_{t1} = \begin{bmatrix} 1 & 0 & 1 & 0 \\ 0 & 1 & 0 & 1 \\ 1 & 0 & 1 & 0 \\ 0 & 1 & 0 & 1 \end{bmatrix}, D_{t2} = \begin{bmatrix} 0 & 1 & 0 & 1 \\ 1 & 0 & 1 & 0 \\ 0 & 1 & 0 & 1 \\ 1 & 0 & 1 & 0 \end{bmatrix},$$

$$D_{t3} = \begin{bmatrix} 1 & 0 & 1 & 0 \\ 0 & 1 & 0 & 1 \\ 1 & 0 & 1 & 0 \\ 0 & 1 & 0 & 1 \end{bmatrix}, D_{t4} = \begin{bmatrix} 0 & 1 & 0 & 1 \\ 1 & 0 & 1 & 0 \\ 0 & 1 & 0 & 1 \\ 1 & 0 & 1 & 0 \end{bmatrix}.$$

506 2) *Compressed Sensing and Block Assembly*: In order to
 507 exploit the sparsity of the JIM DM, CS is applied to all
 508 the dimensions of the joint multi-dimensional matrix symbol
 509 created by the block assembled to increase the throughput. As
 510 shown in Fig. 7, a matrix S_g associated with $N_{vt} = N_v = 4$

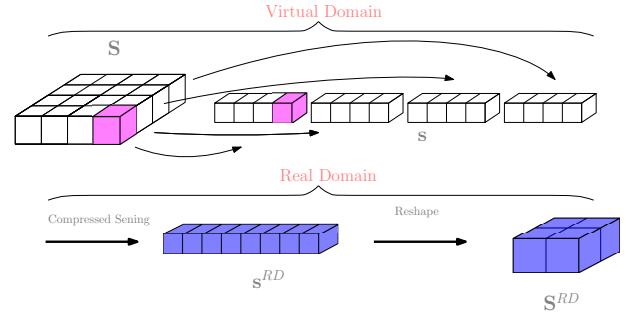


Fig. 7: Illustration of the process for compressing the JMIM DM in the SF domain with $N_{vt} = N_v = 4, K = 1$. Note that this example applies the general JIM with $b_g^1 = [0100]$.

511 will be transformed from the matrix $S, S \in \mathbb{C}^{N_{vt} \times N_v}$ into the
 512 vector $s, s \in \mathbb{C}^{N_{vt} N_v \times 1}$.

513 The symbol vector s is then compressed by a CS measure-
 514 ment matrix $A \in \mathbb{C}^{N_f N_t \times N_v N_{vt}}$ from the $N_v N_{vt}$ -dimensional
 515 s in the VD into the $N_f N_t$ -dimensional form in the Real
 516 Domain (RD)³ denoted as $s^{(RD)}$, which can be written
 517 as: $s^{RD} = As$. The RD vector s^{RD} after CS is then
 518 transferred into a compressed joint multidimensional symbol
 519 matrix $S^{(RD)}$, where $S^{(RD)} \in \mathbb{C}^{N_t \times N_f}$. Then, the index
 520 carrier mapper maps the corresponding joint multidimensional
 521 symbol elements to the OFDM subcarriers and the TAs to form
 522 the SF symbols. Afterwards, G groups of SF symbols S are
 523 assembled by the OFDM creator to a long SF symbol frame, as
 524 shown in Fig. 2. The RD SF symbol can be separated into N_t
 525 FD symbols, which means that N_t FD symbols are transmitted
 526 by N_t TAs. Similar to conventional OFDM, the FD symbol
 527 will be transformed into TD symbols to be transmitted by
 528 their corresponding TAs and then a Cyclic Prefix (CP) will
 529 be added. The G groups of SF symbols S are assembled
 530 by the block creator of Fig. 2 to form a long ST frame,
 531 which is processed by the ST mapper to output a symbol for
 532 transmission over multiple TAs and TSs, Equivalently, the ST
 533 symbols S of each subcarrier group are mapped to N_t TAs
 534 during T TSs, which have N_t symbol sequences $\{s_1, \dots, s_{N_t}\}$
 535 for transmission from the N_t TAs during each TS.

³RD is the joint dimension of DM after the CS process. For instance, the SF-based JMIM signal conveys more bits in the VD than in the RD.

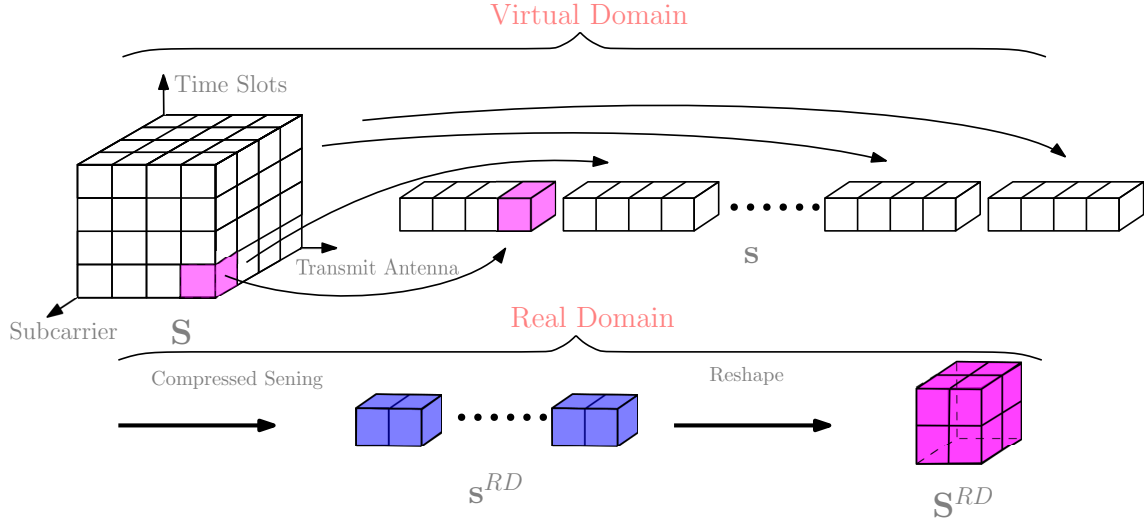


Fig. 8: Illustration of the process for compressing the JMIM DM in the TSF domain with $T = N_t = N_v = 4K = 1$. Additionally, the example presented applies the general JIM for $b_g^1 = [000100]$.

536 For the three-dimensional JMIM, utilizing the TSF dimensions, the TD is also compressed by CS for improving the
 537 throughput, where T_v TSs are introduced in the VD for IM, complemented by T TSs in the TD. Specifically, for the
 538 general JMIM scheme, the TD is introduced for increasing the sparsity and for incorporating extra embedded information
 539 bits. As shown in Fig. 8, we apply CS to the TSF JMIM, where all the three dimensions are compressed for increasing
 540 the throughput. Specifically, a $(4 \times 4 \times 4)$ -sized DM in the VD will be compressed to a $(2 \times 2 \times 2)$ -sized DM of the RD. For
 541 example, when we have $T_v = N_{vt} = N_v = 4$, $b_g^1 = [000100]$ and $K = 1$, the element at the fourth subcarrier, fourth TA
 542 and first TS is activated, corresponding to the coordinate of $(4, 4, 1)$.
 543

544 As for the coded JMIM scheme, additionally the TD is harnessed for further increasing the diversity gain, where CS
 545 is not considered for the TD. We assign either the same or different symbols in a sub-group matrix of the grouped JMIM
 546 scheme, which leads to a different CS approach. Given the different sub-group matrix symbols, the TD is exclusively
 547 harnessed for carrying extra copies of the symbol without CS. The design objective of this scheme is to increase the diversity
 548 gain.
 549

559 B. Receiver Processing

560 As shown in Fig. 9, a receiver having N_r antennas is employed, where we assume that the transmitted signals are
 561 conveyed over a frequency-selective Rayleigh fading channel and the CSI is perfectly acquired at the receiver side. The G
 562 groups of signal are received by the receiver over N_r antennas and then the CP part of the received signals is removed.
 563 Finally, the processed signal is transformed into the FD by using the Fast Fourier Transform (FFT), as shown in Fig. 9.
 564

565 The channel model can be expressed as $\mathbf{h}_\alpha \in \mathbb{C}^{N_r \times N_t}$, which represents the TD CSI between the N_t TAs and the
 566 N_r RAs. Then, the FD channel matrix can be expressed as $\mathbf{H}_\alpha \in \mathbb{C}^{N_r \times N_t}$ for $\alpha = 1, \dots, M$, which are then

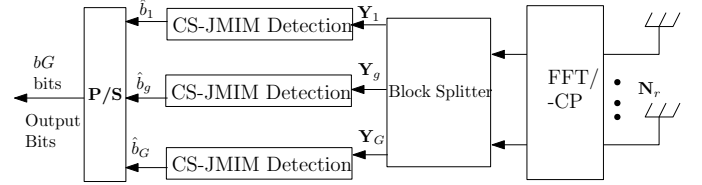


Fig. 9: CS-JMIM system receiver block diagram

572 split into G groups by the Block Splitter of Fig. 9. The symbols received by each subcarrier group are represented as
 573 $\mathbf{Y} = \{\mathbf{Y}[1], \dots, \mathbf{Y}[\alpha], \dots, \mathbf{Y}[N_f]\}$, with $\mathbf{Y} \in \mathbb{C}^{N_r \times N_f}$ and
 574 $\alpha = 1, 2, \dots, N_f$.
 575

576 As for the three-dimensional signal, the transmitted signal is mapped ST symbols, which are also collected by the receiver
 577 and split into G groups by the Block Splitter of Fig. 9. Afterwards, the symbols received in the three dimensions by
 578 each subcarrier group $\mathbf{Y} \in \mathbb{C}^{N_r \times M \times T}$ may be expressed as
 579
 580

$$581 \mathbf{Y} = \left\{ \begin{bmatrix} \mathbf{Y}_{1,1}^1 & \dots & \mathbf{Y}_{1,N_f}^1 \\ \dots & \dots & \dots \\ \mathbf{Y}_{1,1}^{N_r} & \dots & \mathbf{Y}_{1,N_f}^{N_r} \end{bmatrix}_1, \dots, \begin{bmatrix} \mathbf{Y}_{T,1}^1 & \dots & \mathbf{Y}_{T,N_f}^1 \\ \dots & \dots & \dots \\ \mathbf{Y}_{T,1}^{N_r} & \dots & \mathbf{Y}_{T,N_f}^{N_r} \end{bmatrix}_T \right\}. \quad (3)$$

581 The received symbol of the t -th TS can be represented as $\mathbf{Y}_t = \{\mathbf{Y}_t[1], \dots, \mathbf{Y}_t[\alpha], \dots, \mathbf{Y}_t[N_f]\}$, with $\mathbf{Y}_t \in \mathbb{C}^{N_r \times T}$
 582 and $\alpha = 1, 2, \dots, N_f, t = 1, 2, \dots, T$ characterizing the ST structure per group and the ST symbol received at the α -th
 583 subcarrier of each subcarrier group, respectively. Since the index is jointly decided in the multi-dimensional space, we can
 584 transform the ST symbol into a vectorial form \mathbf{y} associated with $\mathbf{y} \in \mathbb{C}^{N_r N_f T \times 1}$.
 585
 586

587 Let the FD channel be $\mathbf{H}_\alpha \in \mathbb{C}^{N_r \times T}$ for $\alpha = 1, \dots, N_f$. Then the signal $\mathbf{Y}_t[\alpha] \in \mathbb{C}^{N_r \times T}$ ($\alpha = 1, \dots, N_f$) received
 588 during the T TSs for each subcarrier group can be expressed as [22]
 589
 590
 591

$$592 \mathbf{Y}[\alpha] = \mathbf{H}_\alpha \mathbf{S}^{(RD)}[\alpha] + \mathbf{W}[\alpha], \quad (4)$$

593 where $\mathbf{S}^{RD}[\alpha] \in \mathbb{C}^{N_r \times T}$ denotes the ST symbols at the sub-
 594 carrier α transmitted from the N_t TAs in the RD. Furthermore,
 595 $\mathbf{W}[\alpha] \in \mathbb{C}^{N_r \times T}$ represents the Additive White Gaussian noise
 596 (AWGN) obeying the distribution of $\mathcal{CN}(0, \sigma_N^2)$, and σ_N^2 is
 597 the noise variance.

598 III. CS-JMIM SIGNAL DETECTION

599 Given the received signal model \mathbf{Y} in (4), the receiver
 600 detects the information bits of the JMIM mapping matrix,
 601 which jointly conveys the index of the active subcarrier, the
 602 active TA and TS in the VD. Firstly, we reshape the received
 603 signal into a vectorial form \mathbf{y} associated with $\mathbf{y} \in \mathbb{C}^{N_r N_f T \times 1}$.

604 The received signal \mathbf{y} contains N_f ST symbols at N_f
 605 subcarriers in the FD of each subcarrier group. Then, we can
 606 rewrite \mathbf{y} with the aid of (4) in the following form:

$$\mathbf{y} = \mathbf{H} \bar{\mathbf{A}} \bar{\mathbf{s}} + \mathbf{w}, \quad (5)$$

607 where $\bar{\mathbf{A}}$ is the equivalent measurement matrix \mathbf{A} used for
 608 compressing the \mathbf{s} VD vectors. In our three-dimensional CS-
 609 JMIM system, $\bar{\mathbf{A}}$ also compresses the TD, where we have
 610 $\bar{\mathbf{A}} \in \mathbb{C}^{N_v t N_v \times N_t N_f}$. Furthermore, $\mathbf{s} \in \mathbb{C}^{N_v N_v t T_v \times 1}$ denotes
 611 the vector of DM combined with the PSK/QAM symbol. In
 612 this case, we could rewrite $\bar{\mathbf{s}}$ in a matrix $\bar{\mathbf{S}}$ associated with
 613 $\bar{\mathbf{S}} = \mathbf{x} \bar{\mathbf{D}}$, where $\bar{\mathbf{D}} \in \mathbb{C}^{N_v \times N_v t \times T_v}$ denotes the realization of
 614 the JMIM DM in each subcarrier group.

615 Conventional exhaustive search based maximum likelihood
 616 (ML) detection can be applied at the receiver, albeit this may
 617 lead to excessive complexity [5]. Furthermore, in the soft
 618 detection scenario, the received signal is converted into prob-
 619 ability values, which are referred to as Log Likelihood Ratios
 620 (LLR) that are fed into the channel decoder for obtaining a
 621 near-capacity performance [43].

622 In the following section we present the conventional ML-
 623 based HD detector, followed by our proposed DNN aided HD
 624 detector, where the neural network replaces the exhaustive
 625 search by a learning-based classification model in order to
 626 significantly reduce the complexity. Afterwards, we discuss
 627 the SD detector, where we first present the conventional SD
 628 detectors followed by our learning-aided SD receiver.

629 A. Hard Decision Decoding

630 Again, we commence with the conventional ML-based
 631 detection of the CS-JMIM system, followed by the DNN-based
 632 detector.

633 1) *Maximum Likelihood Detection*: As shown in Fig. 9,
 634 we detect each group's signal separately. In the CS-JMIM
 635 detector, according to the receiver model of (5), we have
 636 the modified joint JMIM and PSK/QAM symbol, which can
 637 be expressed as $\bar{\mathbf{S}} = \mathbf{x} \bar{\mathbf{D}}$. Here $\bar{\mathbf{D}}$ represents a specific
 638 realization of the selected JMIM DM and \mathbf{x} represents K
 639 STSK PSK/QAM symbols. To detect the specific realization,
 640 we use $\bar{\mathcal{D}}(\beta)$ ($\beta = 1, 2, \dots, N_{JMIM}$) to denote all the possible
 641 realizations of the JMIM DM. Furthermore, as there are
 642 $N_x = (X)^K$ realizations of \mathbf{x} , $\bar{\mathcal{X}}(\gamma)$ ($\gamma = 1, 2, \dots, N_x$) denotes
 643 all the possible realizations of the selected PSK/QAM symbol.

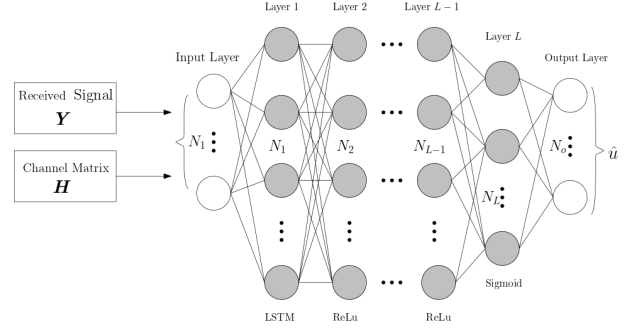


Fig. 10: Fully-connected DNN model for CS-JMIM HD detection.

The ML detector makes a joint decision concerning the JMIM DM and PSK/QAM with the aid of exhaustive search, which can be modelled as

$$\langle \hat{\gamma}, \hat{\beta} \rangle = \arg \min_{\gamma, \beta} \|\mathbf{Y} - \mathbf{H} \bar{\mathbf{A}} \mathcal{X}(\gamma) \bar{\mathcal{D}}(\beta)\|^2, \quad (6)$$

644 where $\hat{\gamma}$ and $\hat{\beta}$ represent the estimates of the selected DM and
 645 the corresponding PSK/QAM constellation in each subcarrier
 646 group, respectively.

The excessively high search complexity of considering all possible candidates by the ML detector is given by $\mathcal{O}[N_{JMIM}(\mathcal{X})^K]$ per subcarrier group.

652 2) *DNN-based Detection*: To reduce the complexity of the
 653 ML detector, learning based detection is considered in this
 654 section, where a DNN based model is proposed for detecting
 655 the received CS-JMIM signal.

656 Detection may also be considered as a classification prob-
 657 lem, where the corresponding bits of the harnessed CS-JMIM
 658 DM and PSK/QAM symbol constitute the DNN output. Under
 659 the assumption of perfect CSI at the receiver side, we use
 660 the received signal and the CSI as the input of the DNN
 661 model. The proposed DNN structure is shown in Fig. 10,
 662 where both the CSI \mathbf{H} at the receiver and the received symbols
 663 \mathbf{Y} constitute the inputs of the L -layer Fully-Connected (FC)
 664 network. Then, the output bits $\hat{\mathbf{u}}$ can be modelled as

$$\hat{\mathbf{u}} = f_{sigmoid}(\mathbf{W}_n \dots f_{Relu}\{\mathbf{W}_2(f_{Relu_1}[\mathbf{W}_1 f_{LSTM}(\mathbf{Y}) + \boldsymbol{\theta}_1]) + \boldsymbol{\theta}_2\} + \dots + \boldsymbol{\theta}_n), \quad (7)$$

666 where \mathbf{W}_n and $\boldsymbol{\theta}_n$, $n = 1, \dots, L$ represent the weights and
 667 biases, respectively. In (7), the Rectified linear unit (Relu)
 668 function of $f_{Relu}(s) = \max(0, s)$ is employed for activating
 669 the DNN during the training phase, while the sigmoid function
 670 of $f_{sigmoid}(s) = \frac{1}{1+e^{-s}}$ is used to obtain the detected bits
 671 $\hat{\mathbf{u}}$. The raw input data represented in the complex-valued
 672 matrix form obtained from the received signal \mathbf{Y} is vectorized
 673 first and then we rearrange the complex values by separately
 674 extracting the real as well as the imaginary parts and then
 675 merging them into a real-valued vector.

676 In the training phase, we employ randomly generated re-
 677 ceived signals, which are transmitted over a frequency selec-
 678 tive Rayleigh fading channel for CS-JMIM. Afterwards, both
 679 the CSI and the received symbols are employed as the input
 680 data of the DNN. The number of training samples required is

681 selected based on experimentation by gradually increasing the
 682 training size until acceptable mean square error (MSE) values
 683 are achieved. In this case, the MSE loss function of the DNN
 684 used for the training is

$$\mathcal{L}(\mathbf{u}, \hat{\mathbf{u}}; \mathbf{W}_n, \boldsymbol{\theta}_n) = \frac{1}{B} \sum_{i=1}^B \|\mathbf{u} - \hat{\mathbf{u}}\|^2, \quad (8)$$

685 where B is the sample size of the current iteration. A stopping
 686 criterion can be defined either by the number of iterations or
 687 by an MSE threshold. Then, the parameter sets $\{\mathbf{W}_n, \boldsymbol{\theta}_n\}$ can
 688 be updated in each training iteration based on our learning
 689 algorithm using gradient descent, which is formulated as

$$\{\mathbf{W}_n, \boldsymbol{\theta}_n\} \leftarrow \{\mathbf{W}_n, \boldsymbol{\theta}_n\} - \alpha \nabla \mathcal{L}(\{\mathbf{W}_n, \boldsymbol{\theta}_n\}),$$

690 where $\alpha > 0$ is the learning rate and $\nabla \mathcal{L}(\{\mathbf{W}_n, \boldsymbol{\theta}_n\})$
 691 represents the gradient of $\mathcal{L}(\{\mathbf{W}_n, \boldsymbol{\theta}_n\})$. In our proposed
 692 network aided detection, we use $\alpha = 0.001$.

693 By the end of the training phase, the DNN has learnt the
 694 mapping from the received signal and stores both the weight as
 695 well as the bias information, which will be used for producing
 696 the desired outputs based on the input data in the testing
 697 phase. The statistical properties of the input/output data have
 698 to remain the same as those used during training.

699 The detection complexity of the learning algorithm is domi-
 700 nated by the calculation of the layer weights and biases, which
 701 may be considered to be of the order of $\mathcal{O}(n_i n_h) + \mathcal{O}(n_h^2) +$
 702 $\mathcal{O}(n_h n_o)$ [29], with n representing the number of neurons in
 703 each layer. Hence, the DNN complexity order is significantly
 704 lower than that of the ML detector.

705 B. Soft Decision Decoding

706 SD detection is employed for attaining near-capacity perfor-
 707 mance, when combined with channel coding. As the computa-
 708 tional complexity of the maximum *a posteriori* probability in
 709 SD detector rapidly increases upon increasing the modulation
 710 order and the number of dimensions [44], the complexity
 711 of CS-JMIM rapidly becomes prohibitive, owing to the joint
 712 detection of JMIM signal in multiple dimensions. In the
 713 following, we present the conventional SD detector of CS-
 714 JMIM, followed by the correspond learning aided SD detector.

715 1) *Conventional Soft Decision Detection*: A channel coded
 716 CS-JMIM scheme is shown in Fig. 11, which was derived from
 717 the CS-MIM model of [22], [36] for achieving near-capacity
 718 performance. A Recursive Systematic Convolutional (RSC)
 719 encoder encodes the information bit sequence \mathbf{b} followed by
 720 an interleaver, where the coded bit sequence \mathbf{c} is interleaved
 721 to generate the stream \mathbf{u} of Fig. 11. Then, the stream \mathbf{u} is
 722 modulated in the CS-JMIM modulator of Fig. 2.

723 At the receiver side of Fig. 11, the received signal \mathbf{Y} and
 724 CSI $\bar{\mathbf{H}}$ are input to the soft CS-JMIM that outputs LLRs.
 725 The LLRs output from the demodulator are then passed to the
 726 de-interleaver and the RSC decoder performs soft decoding. In
 727 Fig. 11, $L(\cdot)$ represents the LLRs of the bit sequences, where
 728 $L_e(u)$ is the output extrinsic LLR after soft demodulation and
 729 $L_a(c)$ is the de-interleaved LLR sequence of $L_e(u)$.

730 The LLR of a bit is defined as the ratio of probabilities
 731 associated with the logical bits '1' and '0', which can be

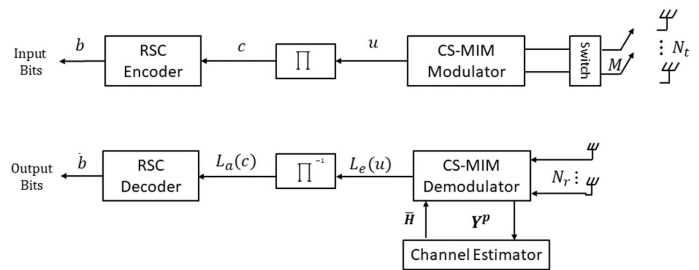


Fig. 11: The transceiver architecture of channel-coded CS-MIM.

written as $L(b) = \log \frac{p(b=1)}{p(b=0)}$. The conditional probability
 $p(\mathbf{Y}|\mathcal{X}_{\beta,\gamma})$ of receiving the group signal \mathbf{Y} is given by [45]

$$p(\mathbf{Y}|\mathcal{X}_{\gamma,\beta}) = \frac{1}{(\pi N_0)^{NT}} \exp\left(-\frac{\|\mathbf{Y} - \mathbf{H}\bar{\mathbf{A}}x(\gamma)\bar{\mathbf{D}}(\beta)\|^2}{N_0}\right), \quad (9)$$

where $\mathcal{X}_{\gamma,\beta}$ represents the PSK/QAM symbol at the β -th CS-
 JMIM DM. Furthermore, N_0 is the noise power, where we
 have $\sigma_n^2 = N_0/2$ with $N_0/2$ representing the double-sided
 noise power spectral density.

Hence, we can formulate the LLR of bit u_i as

$$L_e(u_i) = \ln \frac{p(\mathbf{y}|u_i = 1)}{p(\mathbf{y}|u_i = 0)} = \ln \frac{\sum_{\mathcal{X}_{\gamma,\beta} \in \mathcal{X}_1^i} p(\mathbf{Y}|\mathcal{X}_{\gamma,\beta})}{\sum_{\mathcal{X}_{\gamma,\beta} \in \mathcal{X}_0^i} p(\mathbf{Y}|\mathcal{X}_{\gamma,\beta})}, \quad (10)$$

where \mathcal{X}_1^i and \mathcal{X}_0^i represent a subset of the legitimate equiv-
 alent signal \mathcal{X} corresponding to bit u_i , when $u_i = 1$ and
 $u_i = 0$, respectively, yielding $\mathcal{X}_1^i \equiv \{\mathcal{X}_{\gamma,\beta} \in \mathcal{X} : u_i = 1\}$ and
 $\mathcal{X}_0^i \equiv \{\mathcal{X}_{\gamma,\beta} \in \mathcal{X} : u_i = 0\}$.

Upon using (9) and (10) we obtain the LLR $L(b_i)$ of the bit
 sequence conveyed by the received signal \mathbf{Y} . To simplify the
 calculation, the Approximate Log-MAP (Approx-Log-MAP)
 algorithm based on the Jacobian Maximum operation can be
 used, which is given by [46], [47]

$$L_e(u_i) = \text{jac}_{\mathcal{X}_{\gamma,\beta} \in \mathcal{X}_1^i}(\lambda_{\gamma,\beta}) - \text{jac}_{\mathcal{X}_{\gamma,\beta} \in \mathcal{X}_0^i}(\lambda_{\gamma,\beta}), \quad (11)$$

where $\text{jac}(\cdot)$ denotes the Jacobian maximum operation and the
 intrinsic metric of $\lambda_{\gamma,\beta}$ is

$$\lambda_{\gamma,\beta} = -\|\mathbf{Y} - \mathbf{H}\bar{\mathbf{A}}x(\gamma)\bar{\mathbf{D}}(\beta)\|^2/N_0. \quad (12)$$

At the receiver, the soft demodulator evaluates the prob-
 ability of each bit being logical '1' and '0'. Then it ap-
 plies the approx-log-MAP algorithm for obtaining the extrin-
 sic LLR of the coded bits, which has a complexity order
 $\mathcal{O}[2^{(c_g)}(N_{JMIM}(\mathcal{X})^K)]$, where c_g represents the number of
 coded bits after the RSC encoder and interleaver, and N_{JMIM}
 represents the number of possible realizations of JMIM.

2) *DNN-based SD Detection*: In this section, we propose a
 reduced-complexity SD detector using DNN, which considers
 a similar DNN architecture to that of [29]. Since the conven-
 tional SD detector obtains the LLRs of the received signal
 after the CS-MIM soft demodulator, we replace the detected

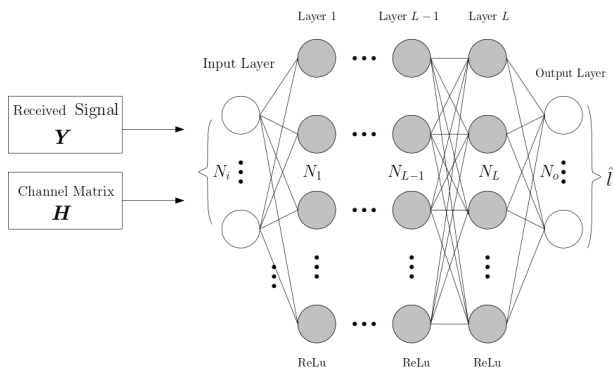


Fig. 12: Fully-connected DNN model for CS-JMIM SD detection.

bits \hat{u} output by the DNN in Fig. 10 with the extrinsic LLR L_e at the output of the DNN, as shown in Fig. 12. Then, the output of the SD DNN model can be expressed as

$$\hat{L}_e = \mathbf{W}_{N_2} \dots f_{Relu} \{ \mathbf{W}_2 (f_{Relu_1} [\mathbf{W}_1 (\mathbf{Y}_\tau + \mathbf{b}_1)] + \mathbf{b}_2 + \dots + \mathbf{b}_{N_2}), \quad (13)$$

and the corresponding loss function is

$$\mathcal{L}(\theta,) = \frac{1}{BT} \sum_{i=1}^B \sum_{t=1}^T \|\hat{L}_e(\tau) - L_e(\tau)\|_2^2. \quad (14)$$

We can also define a stopping criterion, which can be either the number of iterations or meeting a maximum MSE threshold. Then, the parameter sets $\{\mathbf{W}_n, \theta_n\}$ can be updated in each training iteration based on the learning algorithm using gradient descent, which is formulated as

$$\{\mathbf{W}_n, \theta_n\} \leftarrow \{\mathbf{W}_n, \theta_n\} - \alpha \nabla L(\{\mathbf{W}_n, \theta_n\}),$$

where $\alpha > 0$ is the learning rate and $\nabla L(\{\mathbf{W}_n, \theta_n\})$ represents the gradient of $L(\{\mathbf{W}_n, \theta_n\})$.

In our proposed neural network aided detection, we use $\alpha = 0.001$. Similar to the HD DNN detector described above, the model learns the parameters in the training phase and then outputs the LLR information.

The detection complexity of the learning algorithm is dominated by the calculation of the layer weights and biases, which may be considered to be of the order $\mathcal{O}(n_i n_h) + \mathcal{O}(n_h^2) + \mathcal{O}(n_h n_o)$ [29], with n representing the number of neurons in each layer.

IV. ADAPTIVE DESIGN

Since the proposed CS-JMIM design provides flexibility in the design of the JMIM DM, we can design appropriate JMIM DMs for different channel conditions that can provide either an improved BER performance or an increased throughput. Furthermore, in our system, the transmitter can adapt both the JMIM DM \mathcal{D} and the modulation order Q of PSK/QAM. Then, the system throughput may be adapted by appropriately adjusting the above parameters, while maintaining a target BER performance.

In the following two subsections, we highlight the classic threshold-based adaptive modulation, followed by its learning-aided counterpart. More specifically, both the KNN and DNN based adaptive model are applied for the proposed system.

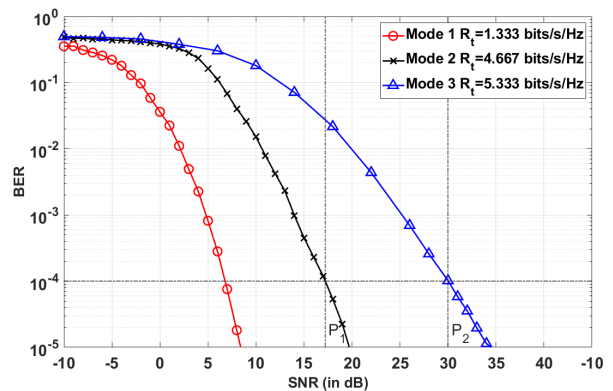


Fig. 13: BER vs. SNR performance of the CS-JMIM system for different mapping modes shown in Table III.

TABLE III: Configuration of the modes presented in Fig. 13

Mode	Mapping Type	Q	N_t	$N_v t$	N_f	N_v	K	R_t
1	Coded	4	4	8	4	8	2	1.333
2	General	4	4	8	4	8	3	4.666
3	Grouped	4	4	8	4	8	1	5.333

1) *Conventional Threshold-based Adaptive Design:* In our adaptive scheme, we can adapt both the configuration of JMIM DM and of the PSK/QAM mode. We can define the different configurations as *Mode1*, *Mode2*, *Mode3*, ..., which can attain different BER performance and throughput. Based on the different modes, the parameters N_v, N_t, T and A of JMIM DM can be selected according to the SNR calculated at the receiver, where the SNR threshold values are selected for the different modes to satisfy a specific target BER [41], [42]. In the following, we present the scenario, where the different adaptive modes P refer to different configurations of the JMIM DM for characterising its design flexibility⁴.

As an example, Fig.13 shows the BER performance of three different CS-JMIM mapping modes. The corresponding parameters and data rates provided by these modes are shown in Table III. For a target BER of 10^{-3} , as shown in Fig. 13 the SNR values of mode transition points P_1 and P_2 can be selected as the thresholds for operating the appropriate modes. Specifically, *Mode1* is applied at low SNR values until the specific SNR reaches P_1 . Then, the mode is changed to *Mode2* to provide higher throughput, when the SNR range spans from P_1 to P_2 . Finally, *Mode3* is selected at SNRs higher than P_2 , which has the highest throughput among the three modes.

For adaptive modulation, the receiver has to confidently infer the choice of the most appropriate transmission mode by comparing the instantaneous SNR of the received symbol against the Mode-switching threshold values. Then, the decision is fed back to the transmitter and applied for the next frame to be transmitted. Generally, with more available operation modes as well as faster and more accurate SNR feed-

⁴Note that the modulation scheme such as PSK/QAM can also be adapted, but in this design example, we aim to show the flexibility of the proposed CS-JMIM design.

back to the transmitter, we can obtain an increased throughput compared to non-adaptive designs. However, threshold-based adaptive modulation design ignores many of the hardware imperfections when deciding upon the threshold values, which results in sub-optimal performance of the adaptive system [41], [42]. Hence, in the next subsection, we propose the learning-based adaptive modulation scheme for our CS-JMIM system to further improve the adaptive system's performance.

2) *Learning aided adaptive modulation*: The adaptive modulation can be modelled as a classification problem, which can be solved using learning-based methods. The SNR of the received signal, which is evaluated at the receiver side, can be fed back to the transmitter and then given the SNR information, which also corresponds to the current channel state information, the transmitter can select a specific mode from a range of candidates to achieve the highest throughput, which still maintain the target BER. Therefore, for a given channel condition, adaptive modulation selects the most suitable mode to achieve the highest throughput, under the constraint of achieving the target BER. In this paper, both the KNN and DNN techniques are investigated in the context of adaptive modulation.

Before the training phase, the input data should be pre-processed to improve the learning efficiency. First, we randomly generate the training data of each mode under different instantaneous SNR values at the receiver. Then, the corresponding switching SNRs that can maintain a BER lower than the target BER are stored. Given these training data, we can use learning models to find the mode switching thresholds in the training phase. After training, the trained model becomes capable of predicting the next mode, given the knowledge of the SNR. In the following, we first employ KNN for our adaptive modulation scheme and then we propose a DNN-based adaptive model for further improving the performance.

a) *KNN-based Adaptive Design*: KNN is a popular classification techniques relying on low-complexity implementation and yet providing a good performance [48]. Yang *et al.* [40] developed KNN-assisted adaptive modulation schemes for SM, while Liu *et al.* [41] further developed DNN aided adaptive modulation to millimeter wave communication. To elaborate briefly on the KNN process, we define the training sets as

$$\mathcal{T}^{(i)} = [\xi_1^{(i)}, \dots, \xi_n^{(i)}, \dots, \xi_{N_p}^{(i)}]^T, \quad (15)$$

where ξ represents the SNR value of a symbol with a BER lower than the target BER value, with $i = 1, 2, \dots, \mathcal{I}$ representing the adaptive mode index and N_p is the total number of instantaneous SNR values with BER under the target. Then, the total training set of each mode can be formulated as

$$\mathcal{T} = [\mathcal{T}^{(1)}, \dots, \mathcal{T}^{(i)}, \dots, \mathcal{T}^{(I)}]^T. \quad (16)$$

During runtime, for a given new data point, which corresponds to the instantaneous SNR ξ , the KNN model finds k nearest neighbours in the training set \mathcal{T} , using a distance metric $d(\cdot)$, which can be expressed as

$$d(\xi_n^{(i)}, \xi_{new}) = \|\xi_n^{(i)} - \xi_{new}\|^2. \quad (17)$$

Then, the mode is decided by the majority mode of the k nearest neighbours to the input test point. With the possibility

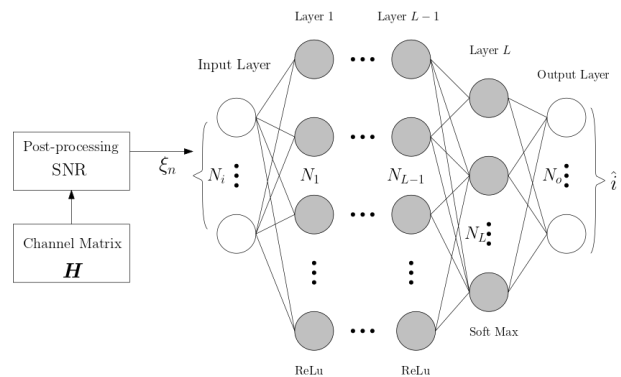


Fig. 14: Fully-connected DNN model for CS-MIM adaptive modulation selection.

of several modes having the same number in the k nearest neighbours, the mode with the highest throughput will be selected.

The performance of KNN significantly depends on its parameters and on the value of k , where the best value of k can be selected empirically. In this adaptive system, the best value of k is determined by considering the trade-off between the BER and throughput. Furthermore, KNN results in a high computational complexity for the nearest neighbour search in addition to requiring a large memory for storing the training. Hence, in the following we present a DNN based design alternative.

b) *DNN-aided Adaptive Design*: In this section, we present the DNN-based adaptive modulation regime of Fig. 14. Similarly to KNN, we randomly generate the training data and then store the mode index and SNR value pairs, which have BERs lower than the target value. Then, the training set \mathcal{T} constitutes the estimated SNR ξ of a symbol associated with a BER lower than the target BER. We use the DNN-based classification model, where the input corresponds to the instantaneous SNR and the output corresponds to the mode index of adaptive modulation.

The output mode index \hat{i} of the DNN can be expressed as

$$\hat{i} = f_{softmax}(\mathbf{W}_n \dots f_{Relu}\{\mathbf{W}_2(f_{Relu_1}[\mathbf{W}_1\xi + \boldsymbol{\theta}_1]) + \boldsymbol{\theta}_2\} + \dots + \boldsymbol{\theta}_n), \quad (18)$$

where \mathbf{W}_n and $\boldsymbol{\theta}_n$, $n = 1, \dots, L$ represent the weights and biases, respectively. Relu is also employed for activating the DNN during the training phase, and the softmax function is used to obtain the mode index \hat{i} , which is

$$f_{softmax}(s) = \frac{e^s}{\sum_{c=1}^C e^{s_c}}. \quad (19)$$

The number of training samples required is selected based on experimentation by gradually increasing the training size until acceptable MSE values are achieved. In this case, the MSE loss function of the DNN used for the training is

$$\mathcal{L}(\xi, \hat{\xi}; \mathbf{W}_n, \boldsymbol{\theta}_n) = \frac{1}{B} \sum_{i=1}^B \|\xi - \hat{\xi}\|^2, \quad (20)$$

where B is the sample size of the current iteration.

TABLE IV: CS-MIM system simulation parameters.

Parameters	Scheme 1	Scheme 2	Scheme 3	Scheme 4	Scheme 5	Scheme 6	Scheme 7	Scheme 8	Scheme 9	
Scheme type	CS-GFIM-SM	CS-JMIM	CS-GFIM-SM	CS-JMIM	CS-MIM	CS-JMIM				
Detection type	HD						SD			
Multi-carrier System	OFDM									
Number of subcarriers, N_c	128									
Cyclic prefix	16									
Num of subcarrier group, G	64		32		1,2		64			
Num of active indices/gp, K	1,2		1,2,3		1,2		2			
Receiver antennas, N_r	2		4		8		2			
RSC code, (n, k, K)							(2,1,3)			
Real Domain										
Num of subcarrier/group, N_f	2		4		8		2			
Transmit antennas, N_t	2		4		8		2			
Activated antennas, N_{at}	1	-	1	-	2					
Time Slots, T						2				
Virtual Domain										
Num of available subcarrier/group, N_v	8	4	16	8	8	4				
Transmit antennas, N_{vt}	-	4	-	8	-	2				
Time Slots, T_v						4				
STSK codeword, (m, n, t, q, l)	-				(2,2,2,2,4)		-			

912 A stopping criterion can be defined either by the number of
913 iterations or by the maximum tolerable MSE threshold. Then,
914 the parameter sets $\{\mathbf{W}_n, \boldsymbol{\theta}_n\}$ can be updated in each train-
915 ing iteration based on our learning algorithm using gradient
916 descent, which is formulated as

$$\{\mathbf{W}_n, \boldsymbol{\theta}_n\} \leftarrow \{\mathbf{W}_n, \boldsymbol{\theta}_n\} - \alpha \nabla L(\{\mathbf{W}_n, \boldsymbol{\theta}_n\}),$$

917 where $\alpha > 0$ is the learning rate and $\nabla L(\{\mathbf{W}_n, \boldsymbol{\theta}_n\})$
918 represents the gradient of $L(\{\mathbf{W}_n, \boldsymbol{\theta}_n\})$. In our proposed
919 DNN-aided detection, we use $\alpha = 0.001$.

920 V. SIMULATION RESULTS AND ANALYSIS

921 In this section, we characterize the performance of the
922 proposed CS-JMIM system, where conventional detection will
923 be used for benchmarking the proposed learning aided detec-
924 tion methods. Furthermore, we consider the system employing
925 SF CS-JMIM and TSF CS-JMIM. The BER performance
926 is evaluated by Monte-Carlo simulations, where we use the
927 simulation parameters summarized in Table IV. The parameters
928 used by the learning models are presented in Table VI. In our
929 simulations, we assume that the receiver has perfect channel
930 knowledge, while in practice this is estimated using channel
931 estimation techniques.

932 In the following, we present the different schemes consid-
933 ered in our simulations for comparison purposes. Firstly,
934 we compared CS-aided separate multi-dimensional IM with
935 CS-JMIM. More specifically, for our SF domain system, we
936 compared CS-aided Generalized Subcarrier Index Modulation
937 with SM (CS-GFIM-SM). These are termed as **Scheme 1, 3**,
938 with CS-JMIM as **Scheme 2, 4**. Then, for the TSF domain,
939 the CS-JMIM of **Scheme 5** is compared to **Scheme 6**, which
940 represents the CS-MIM [22] [36]. Secondly, we compared the
941 performance of different parameters in the context of **Schemes**
942 **2, 4, 6**. Thirdly, we characterized the performance of DNN-
943 aided CS-JMIM both in HD and SD in **Schemes 6-9**. We also
944 quantified the complexity and compared it to conventional ML
945 detection. Finally, we also exploited the adaptation of CS-
946 JMIM between different JMIM methods in **Scheme 10**. To
947 elaborate:

948 1) **Scheme 1**: applies ML HD detection for the CS-GFIM-
949 SM, which activated one of 2 TAs, 2 RAs, and 2

subcarriers per group, while considering 8 subcarriers 950
per group in the VD and $K = 1, 2$ activated subcarriers. 951

2) **Scheme 2**: applies maximum likelihood hard decision 952
detection for the CS-JMIM system in the SF domain 953
along with 2 TAs, 2 RAs, and 2 subcarriers per group in 954
the RD, while considering 4 antennas and 4 subcarriers 955
per group in the VD. In this scheme, we consider the 956
following mappings: 957

- a) General JMIM with $K = 1, 2$. 958
- b) Grouped JMIM with $gs = 4$ subgroups, and each 959
subgroup applies general JMIM in conjunction 960
with $K = 1$ (In this case, we can consider that 961
both the FD and SpD is split into two sub groups, 962
which have $gsx = gsy = 2$). 963
- c) Coded JMIM with $n_q = 2$. 964

3) **Scheme 3**: applies ML HD detection for the CS-GFIM- 965
SM, which activated one antenna out of 4 TAs, 4 966
RAs, and 4 subcarriers per group, while considering 967
16 subcarriers per group in the VD and $K = 1, 2, 3$ 968
activated subcarriers. 969

4) **Scheme 4**: applies maximum likelihood hard decision 970
detection for the CS-JMIM system in the SF domain 971
along with 4 TAs, 4 RAs, and 4 subcarriers per group 972
in this RD, with 8 antennas and 8 subcarriers per group 973
in the VD. In this scheme, we consider the following 974
mappings: 975

- a) General JMIM with $K = 1, 2, 3$. 976
- b) Grouped JMIM with $gs = 4, gsx = gsy = 2$ sub- 977
groups, with each subgroup applying the general 978
JMIM along with $K = 1$. 979
- c) Coded JMIM with $n_q = 4$ 980

5) **Scheme 5**: applies ML HD detection for the CS-MIM 981
system in the TSF domain with 8 TAs, 8 RAs, 2 sub- 982
carriers per group and 2 TSs, while having 8 subcarriers 983
per group in the VD. For the Space-Time-Shift-Keying 984
(STSK) codeword $STSK(M, N, T, Q, L)$ used in CS- 985
MIM [22], STSK(2,2,2,2,4) is applied. In this case, 986
we have 2 activated antennas out of 8 and $K = 1, 2$ 987
activated subcarrier out of 8 subcarrier in the VD. 988

6) **Scheme 6**: applies maximum likelihood hard decision 989

TABLE V: Simulation results and complexity analysis of each Scheme.

Scheme index		SNR at BER of 10^{-5}	Throughput(bits/s/Hz)	Complexity	
HD Detection					
Scheme 1		K=1	20.8	2.667	1.4×10^5
		K=2	26.5	4	5.6×10^5
Scheme 2	a)	K=1	30.3	2.667	9.5×10^5
		K=2	30.2	4.444	3.8×10^6
	b)		34.9	7.111	5.1×10^8
	c)		22.4	1.778	1.8×10^5
Scheme 3		K=1	16.6	1.778	8.6×10^6
		K=2	23.4	2.667	3.4×10^7
		K=3	28.1	3.778	1.4×10^8
Scheme 4	a)	K=1	8.2	1.778	5.3×10^7
		K=2	13.4	3.111	2.1×10^8
		K=3	19.4	4.667	8.3×10^8
	b)		34.6	5.333	2.2×10^{10}
	c)		8.3	1.333	7.2×10^6
Scheme 5		K=1	9.6	3.556	1.2×10^7
		K=2	13.3	5.333	4.9×10^7
Scheme 6	a)	K=1	-0.4	3.556	4.1×10^7
		K=2	4.9	6.222	6.5×10^9
	b)		15.7	17.778	5.4×10^{11}
	c)		1.5	1.778	1.1×10^7
Scheme 7	a)		5.6	3.556	2.2×10^5
	b)		18.7	17.778	1.7×10^6
	c)		1.8	1.778	6.6×10^4
SD Detection					
Scheme 8	a)		1.1	1.778	2.2×10^{13}
	b)		6.2	8.889	3.2×10^{14}
	c)		0.1	0.889	3.4×10^{12}
Scheme 9	a)		4.3	1.778	1.3×10^6
	b)		8.9	8.889	8.3×10^6
	c)		4.1	0.889	1.2×10^5
Adaptive Modulation					
Scheme 10	a)		-	-	-
	b)		-	-	5.2×10^6
	c)		-	-	1.22×10^5

TABLE VI: Training configuration for learning-aided detection method of Scheme 7,9

Setting	Hard-decision	Soft-decision
Maximum training epoch	400	1000
Initial learning rate	0.001	
Target SNR for training	0dB-20dB	-10dB to 5dB
Mini batch size	1000	200 to 500
Optimizer	Adam	
Training data size	50000	
Validation data ratio	0.1	

TABLE VII: Training configuration for adaptive modulation of Scheme 10

Setting	value
Number of Channel realizations for training	100000
Number of Channel realizations for testing	20000
Target SNR for training	0dB-30dB
Number of neighbors in KNN searchin k	15
Number of FC layers in DNN	3
Number of neurons in each FC layer	(128,256,128)
Number of output layer size	3
Activation function for output layer	Soft Max

990 detection for the CS-JMIM system in the TSF domain
 991 with 2 TAs, 2 RAs, 2 subcarriers per group and 2 TSs in
 992 the RD, while using 4 antennas, 4 subcarriers per group
 993 and 4 TSs in the VD. In this scheme, we consider the
 994 following mappings:

- a) General JMIM with $K = 1, 2$. 995
 b) Grouped JMIM with $gs = 8, gsx = gsy = gsz =$ 996
 2 subgroups, where each subgroup applies general 997
 JMIM along with $K = 1$.(In this case, we further 998
 split the TD into two parts, which have $gsz = 2$.) 999
 c) Coded JMIM $n_q = 2$. 1000
- 7) **Scheme 7:** applies DNN based HD detection for the 1001
 CS-JMIM system. Here, we consider 2 TAs, 2 RAs, 2 1002
 subcarriers per group, and 2 TSs in the RD, while using 1003
 4 antennas, 4 subcarriers per group and 4 TSs in the VD. 1004
 In this scheme we consider the following mappings: 1005
- a) General JMIM with $K = 2$. 1006
 b) Grouped JMIM with $gs = 8, gsx = gsy = gsz =$ 1007
 2 subgroups, where each subgroup applies general 1008
 JMIM with $K = 1$. 1009
 c) Coded JMIM with $n_q = 2$. 1010
- 8) **Scheme 8:** applies conventional SD detection for the 1011
 CS-JMIM system in the TSF domain, while using RSC 1012
 channel coding RSC(2,1,3). Here, we consider 2 TAs, 1013
 2 RAs, 2 subcarriers per group, and 2 TSs in the RD, 1014
 while using 4 antennas, 4 subcarriers per group and 4 1015
 TSs in the VD. In this scheme, we consider the following 1016
 mappings: 1017
- a) General JMIM with $K = 2$. 1018
 b) Grouped JMIM with $gs = 8, gsx = gsy = gsz =$ 1019

- 1020 2 subgroups, each subgroup applied general JMIM
1021 with $K = 1$.
1022 c) Coded JMIM with $n_q = 2$.
- 1023 9) **Scheme 9**: applies DNN-based SD detection for the CS-
1024 JMIM system in the TSF domain, while using RSC
1025 channel coding RSC(2,1,3). Here, we consider 2 TAs,
1026 2 RAs, 2 subcarriers per group, and 2 TSs in the RD,
1027 while using 4 antennas, 4 subcarriers per group and 4
1028 TSs in the VD. In this scheme, we consider the following
1029 mappings:
1030 a) General JMIM with $K = 2$.
1031 b) Grouped JMIM with $gs = 8, gsx = gsy = gsz =$
1032 2 subgroups, each subgroup applied general JMIM
1033 with $K = 1$.
1034 c) Coded JMIM with $n_q = 2$.
- 1035 10) **Scheme 10**: Adaptive HD-CS-JMIM system based on
1036 the TSF domain with 2 TAs, 2 RAs, 2 subcarriers per
1037 group, 2 TSs in RD and 4 antennas, 4 subcarriers per
1038 group and 4 TSs in VD. The details of the DNN based
1039 adaptive system design are shown in Table VII. In this
1040 system, we consider the following adaptation schemes:
1041 a) Conventional adaptation.
1042 b) KNN-based adaptation.
1043 c) DNN-based adaptation.

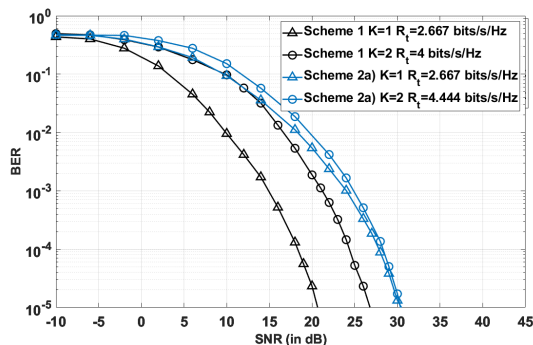


Fig. 15: BER performance comparison of Scheme 1 and Scheme 2a). Our simulation parameters are shown in Table IV.

- 1044 As shown in Fig. 15, we compared the CS-aided separate
1045 MIM - namely the CS-GFIM-IM in this case - to CS-JMIM,

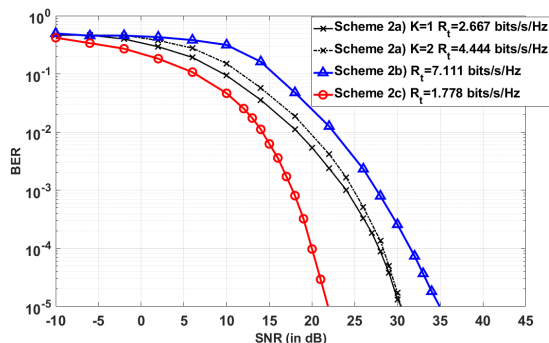


Fig. 16: BER performance comparison of CS-JMIM Scheme 2. Our simulation parameters are shown in Table IV.

1046 which applied the general JMIM method of Section II-A1a).
1047 In this case, based on the transmission rate calculation formula
1048 $\frac{bG}{N_c + L_{CP}}$, we have the transmission rate of the CS-GFIM-
1049 IM associated with $K = 1$ in **Scheme 1** as $R_t^{k=1} = 2.667$
1050 bits/s/Hz. This is the same as the CS-JMIM associated with
1051 $K = 1$ in **Scheme 2a)** under identical hardware configuration.
1052 However, the performance of **Scheme 2a)** is almost 10 dB
1053 worse than that of **Scheme 1** at a BER of 10^{-5} . Hence CS-
1054 JMIM is unattractive in this situation. For more activated index
1055 entities of both CS-JMIM and CS-GFIM-IM, the throughput
1056 of **Scheme 1** is increased to $R_t^{1,k=2} = 4$ bits/s/Hz and **Scheme**
1057 **2a** has $R_t^{2,k=2} = 4.444$ bits/s/Hz. In this case, **Scheme 2a** of
1058 $K = 2$ has a 3.6 dB better performance than **Scheme 1** of
1059 $K = 2$ at a BER of 10^{-5} .

1060 Fig. 16 shows the performance of the proposed CS-JMIM
1061 **Scheme 2** for different JMIM methods. Observe that for a
1062 small index space of $N_t = N_f = 2$, the detector cannot
1063 beneficially exploit the sparsity. The transmission rate of
1064 **Scheme 2** is either $R_t^{k=1} = 2.667$ bits/s/Hz, or $R_t^{k=2} = 4.444$
1065 bits/s/Hz and we have $R_t^b = 7.111$ bits/s/Hz, $R_t^c = 1.778$
1066 bits/s/Hz. As shown in Fig. 16, **Scheme 2a)** associated with
1067 $K = 1, 2$ has a similar BER performance, while **Scheme 2a)**
1068 of $K = 2$ has a higher throughput. Additionally, **Scheme 2b)**
1069 has almost 4 times the transmission rate compared to **Scheme**
1070 **2c)**, but the latter has an increased diversity gain. Hence the
1071 BER performance of **Scheme 2c)** is 12dB better than that of
1072 **Scheme 2c)**.

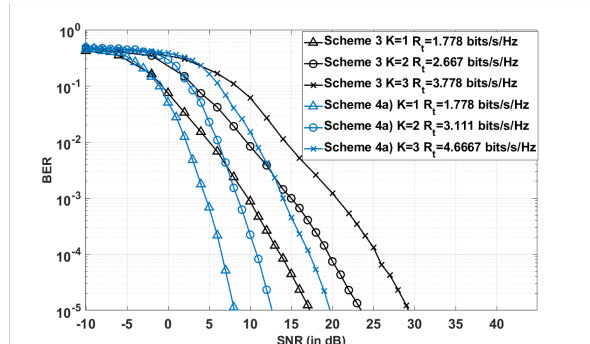


Fig. 17: BER performance comparison of Scheme 3 and Scheme 4a). Our simulation parameters are shown in Table IV.

1073 To further exploit the sparsity of CS-JMIM, we also consider
1074 larger SF dimensions applied to the JMIM method, as shown in
1075 Fig. 17. We assume that both schemes have the same number of
1076 TAs and subcarriers per group along with an adjustable number of
1077 VD subcarriers. For $N_t = 4, N_f = 4$, the CS-JMIM of **Scheme**
1078 **4a)** achieves better performance than the separate MIM in **Scheme**
1079 **3** with the same K value. Specifically, both schemes have
1080 $R_t^{k=1} = 1.777$ bits/s/Hz and **Scheme 3** associated with $K = 1$
1081 obtains 5 dB SNR gain over **Scheme 4a)** with $K = 1$ at BER of
1082 10^{-5} . When relying on a higher K , CS-JMIM is capable of
1083 providing higher throughput as well as improved detection
1084 performance. With $K = 2, 3$, the throughput of **Scheme 3** is
1085 $R_t^{k=2} = 2.667$ bits/s/Hz and $R_t^{k=3} = 3.333$ bits/s/Hz, respectively,
1086 while **Scheme 4a)** could achieve $R_t^{k=2} = 3.111$ bits/s/Hz and
1087 $R_t^{k=3} = 4.667$ bits/s/Hz.

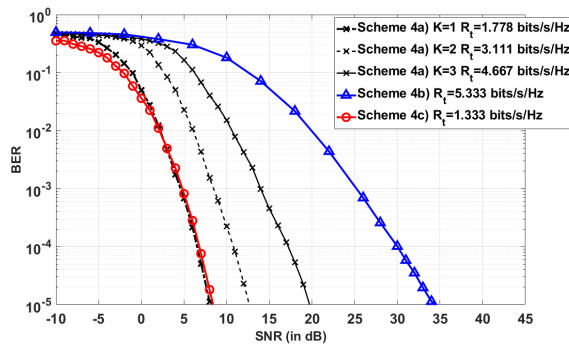


Fig. 18: BER performance comparison of CS-JMIM Scheme 4. Our simulation parameters are shown in Table IV.

1088 Fig. 18 shows the BER performance of **Scheme 4**. A
 1089 higher VD index mapping DM size allows for more flexible
 1090 K value selection in **Scheme 4a)**. Observe that **Scheme 4a)**
 1091 with $K = 1$ achieves a similar performance to **Scheme 4c)**,
 1092 where **Scheme 4a)** with $K = 1$ has $R_t = 1.778$ bits/s/Hz and
 1093 **Scheme 4c)** has $R_t = 1.333$ bits/s/Hz.

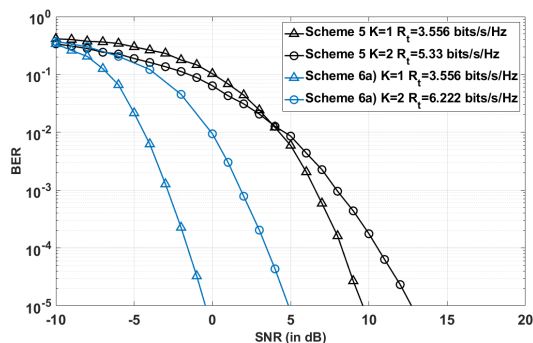


Fig. 19: BER performance comparison of Scheme 5 and Scheme 6a). Our simulation parameters are shown in Table IV.

1094 For the TSF domain system of Fig.6(a), we consider a
 1095 separate model termed as CS-MIM [22]. This model applied
 1096 SIM and STSK in the FD and CS is applied for the FD. Then
 1097 the symbol after IFFT is modulated using SM and transmitted
 1098 by the activated antennas. The CS-MIM scheme is simulated
 1099 using the parameters of Table IV for **Scheme 5**. In this case,
 1100 to achieve the same throughput as **Scheme 5** and **Scheme 6a)**
 1101 at $K = 1$, for **Scheme 5**, we deliver the signals over 8 TAs
 1102 with the aid of 2 RF chains. Then both **Scheme 5** and **Scheme**
 1103 **6a)** can have a throughput of $R_t^{K=1} = 3.556$ bits/s/Hz with
 1104 $K = 1$. Then, we can observe in Fig.19 that **Scheme 6a)**
 1105 achieves a BER of 10^{-5} at -0.1 dB while **Scheme 5** requires
 1106 about 9.8 dB at the same BER. For $K = 2$, **Scheme 5** requires
 1107 13.5 dB SNR at 10^{-5} BER for $R_t^{K=2} = 5.333$ bits/s/Hz and
 1108 **Scheme 6a)** requires 7.5 dB lower SNR than **Scheme 5** for
 1109 $R_t^{K=2} = 6.222$ bits/s/Hz.

1110 In Fig. 20, the TSF domains are considered for the
 1111 CS-JMIM using **Scheme 6**. As shown in Fig. 20, **Scheme**
 1112 **6a)** with $K = 1$ attains the best performance among all
 1113 types in **Scheme 6**. Quantitatively, at a BER of 10^{-5} ,
 1114 it requires an SNR of -0.3 dB and has a throughput of

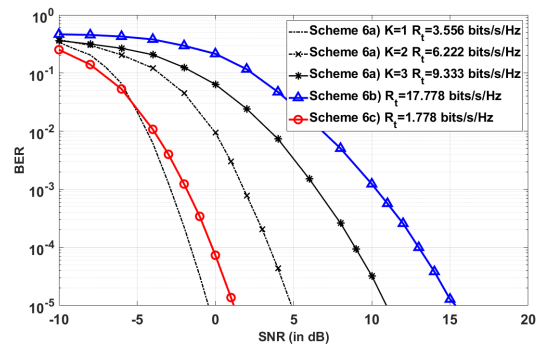


Fig. 20: BER performance comparison of CS-JMIM Scheme 6. Our simulation parameters are shown in Table IV.

1115 $R_t = 3.556$ bits/s/Hz. **Scheme 6c)** achieves a BER of 10^{-5}
 1116 at an SNR of 1.1 dB. When higher dimensions are introduced,
 1117 both the general JMIM and grouped JMIM can provide a
 1118 high throughput as well as a good BER performance, albeit
 1119 at the cost of a huge detection complexity. In Fig. 20,
 1120 **Scheme 6b)** represents the grouped JMIM associated with
 1121 8 sub-groups. When $K = 1$ and the general JMIM DM
 1122 is applied, we have $R_t = 17.778$ bits/s/Hz. This scheme
 1123 attains a BER of 10^{-5} at an SNR of 15.1 dB. **Scheme**
 1124 **6a)** with $K = 3$ has $R_t = 9.333$ bits/s/Hz and achieves
 1125 a BER of 10^{-5} at an SNR of 11 dB. Hence, for higher
 1126 dimensions, the grouped JMIM outperforms the other
 1127 two JMIM methods. However, the complexity of grouped
 1128 JMIM is exponentially increasing. Specifically, the detection
 1129 complexity order of the grouped JMIM can be expressed as
 1130 $\mathcal{O}[(N_{JMIM}(\mathcal{X}^K))^{N_{sub}}]$ for the TSF domain CS-JMIM system.
 1131 This can be simplified to $\mathcal{O}[(N_v N_{vt} T_v / (g_s)) (M^K)^{N_{sub}}]$,
 1132 where N_{sub} represents the number of sub-groups. On the
 1133 other hand, the detection complexity order of the general
 1134 JMIM is $\mathcal{O}[(N_v N_{vt} K T_v M^K)]$. Furthermore, the coded
 1135 JMIM complexity order can be $\mathcal{O}[(N_q - n_q) n_q M]$. Then we
 1136 can formulate the computational complexity order of ML
 1137 for **Scheme 7a)** as $\mathcal{O}_{ML}[N_r N_f N_t T (N_r N_f N_t T N_{vt}^2 N_v^2 T_v^2 +$
 1138 $N_{vt} N_v T_v M^2 N_f N_t T + MK)(N_{JMIM}(\mathcal{X}^K))]$. For
 1139 **Scheme 7b)**, the sub-groups must be considered
 1140 in each rounds, which have a complexity of
 1141 $\mathcal{O}_{ML}[(N_{sub} N_r N_f N_t T / g_s) (N_r N_f N_t T N_{vt}^2 N_v^2 T_v^2 / (g_s^2) +$
 1142 $N_{vt} N_v T_v M N_f N_t T M / g_s + MK)(N_{JMIM}(\mathcal{X}^K))^{N_{sub}}]$.
 1143 For **Scheme 7c)**, we have a reduced complexity order of
 1144 $\mathcal{O}_{ML}[N_r N_f N_t T N_{vt} N_v T_v M N_f N_t T M (N_q - n_q) n_q M]$
 1145 due to having multiple bit copies. Then we can calculate the
 1146 computational complexity based on Table IV, as shown in
 1147 Table V.

1148 Upon increasing the throughput excessive detection complex-
 1149 ity is imposed by conventional ML detection. To reduce
 1150 the detection complexity, we have to accept a performance vs.
 1151 complexity trade-off. In this context, we compare our DNN-
 1152 based detector of the TSF based CS-JMIM system to conven-
 1153 tional maximum likelihood detection by comparing **Scheme 6**
 1154 and **Scheme 7** in Fig 21. Observe that the DNN-assisted HD
 1155 detector achieves a similar performance to the ML detector.
 1156 Furthermore, the complexity of the NN is determined by that

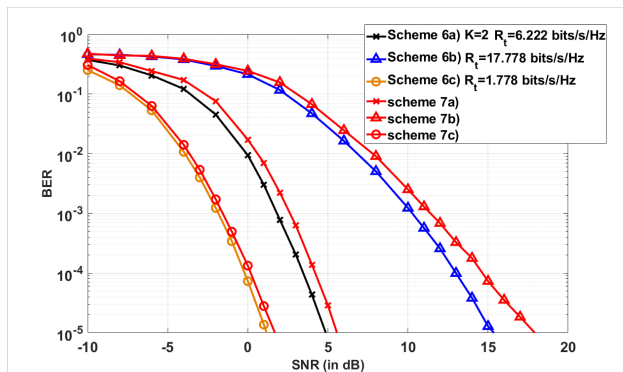


Fig. 21: BER performance comparison of CS-JMIM Scheme 6 and Scheme 7. Our simulation parameters are shown in Table IV.

of the forward and backward propagation, where we have the general DNN complexity order of $\mathcal{O}[n_i n_l n_{l+1} n_{h_L} n_o]$. Here n_i and n_o denote the number of neurons in the input and output layers, $n_l (l = 1, 2, \dots)$ is the number of neurons in the hidden layer between the input and output. Then we can analyse each DNN model in **Scheme 8**. For a classification neural network, we have the LSTM layer as the activation layer of the input layer, which has the complexity of $\mathcal{O}_{LSTM}[4n_l(n_d + 2 + n_l)]$, where n_d is the number of neurons in the input layer and the popular sigmoid function is used as the activation layer of the output layer. The associated complexity is $\mathcal{O}[2n_L n_{L-1} - n_{L-1} + 2n_{L-1}]$. The complexity of the FC layer with the ReLu function is given by $\mathcal{O}[2n_l n_{l-1} - n_{l-1} + 1]$. Then we have the computational complexity order of $\mathcal{O}[4n_l(n_1 + 2 + n_l) + \sum^L -1_l(2n_{l+1}n_l - n_l) + 2n_{L-1}]$. Now we can also summarize the computational complexity of the DNN methods in Table V.

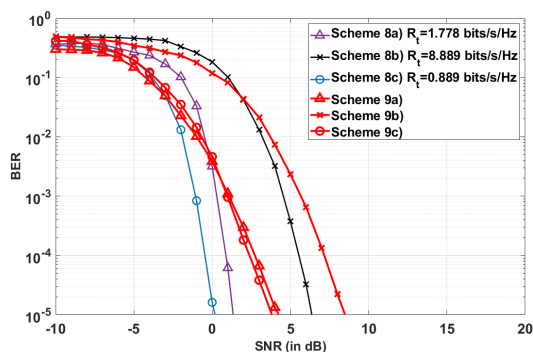


Fig. 22: BER performance comparison of CS-JMIM Scheme 8 and Scheme 9. Our simulation parameters are shown in Table IV.

Furthermore, we extend the DNN-assisted detector to the SD of the TSF domain CS-JMIM system in **Scheme 8** and **Scheme 9**, while using the half-rate RSC encoder RSC(2,1,3), having a memory of 3. As shown in Fig. 22, with the aid of channel coding, the performance of CS-JMIM can be further increased, as seen for **Scheme 8**. By comparing **Scheme 8** of

TABLE VIII: Configuration of mode used in conventional adaption with TSF domain CS-JMIM

No	Type	Scheme	R_t
1	Coded	Scheme 7a)	1.778
2	General	Scheme 7b)	6.222
3	Grouped	Scheme 7c)	17.778

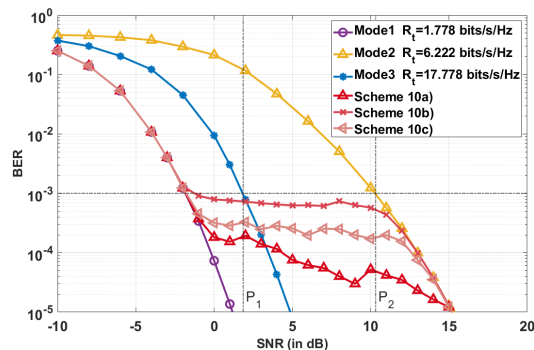


Fig. 23: Adaptive modulation performance comparison of CS-JMIM Scheme 7. Our simulation parameters are shown in Table IV.

Fig. 22 and **Scheme 6** of Fig. 21, the detection performance is 1dB better for **Scheme 8c**) than for **Scheme 6c**) at the BER of 10^{-5} . Furthermore, **Scheme 8a**) requires an SNR of 6.2 dBs at BER= 10^{-5} , while **Scheme 6a**) necessitates SNR=1.6 dB. **Scheme 8b**) has the best performance, outperforming **Scheme 6b**) by about 8 dB at a BER of 10^{-5} . Fig.22 also shows the performance of DNN based detection for TSF CS-JMIM, where **Scheme 9a**) and **Scheme 9c**) exhibit similar performance. Quantitatively, they require about 4 and 3.2 dB at a BER of 10^{-5} . **Scheme 9b**) requires 3 dB higher SNR than the conventional SD detector, but it is still about 6 dB better than **Scheme 7b**). The proposed learning method has a complexity order of $\mathcal{O}[\mathcal{O}(n_i n_l) + \mathcal{O}(n_l^2) + \mathcal{O}(n_l n_o)]$ compared to $\mathcal{O}[2^{c_g} (T_v N_t N_{vt} (Q\mathcal{X})^K)]$ for the conventional scheme, where c_g denotes the RSC-coded number of bits in a transmitted symbol.

Finally, we present the performance of **Scheme 10** in

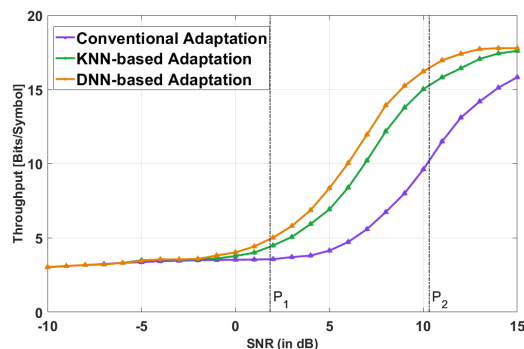


Fig. 24: Adaptive modulation performance comparison of CS-JMIM Scheme 7. Our simulation parameters are shown in Table IV.

Fig. 23. For the sake of a fair comparison, we use the data sets of the same size for both training and testing the KNN and DNN-based systems. Table VIII presents the configurations of the three modes of operation used in the adaptive system simulated. The switching thresholds for the conventional adaptive modulation are set as $P_1 = 1.85$ dB and $P_2 = 10.3$ dB, as shown in Fig. 23. Specifically, the conventional adaptive modulation scheme characterized in Fig. 23 uses $Mode_1$ when $SNR < P_1$, and $Mode_2$ for $P_2 > SNR$. After the instantaneous SNR becomes higher than P_2 , $Mode_3$ is selected. Again, our KNN-based and DNN-based mode-selection algorithms are used in Fig. 23. Observe that the DNN based adaptive system attains a BER closer to the target of 10^{-3} than the KNN based adaptive system. Then we can further analyse the throughput of each mode selection scheme in Fig. 24. Observe that the DNN-based adaptive modulation scheme achieves a higher throughput than the KNN-based one, because more accurate decisions can be made by the DNN classifier than by the KNN classifier. Clearly, the learning assisted adaptive schemes are capable of selecting the best possible mode, while the conventional adaptive modulation uses the predefined average SNR-based thresholds for mode selection.

VI. CONCLUSIONS

A CS-JMIM system was proposed and DL-aided detection using both HD and SD was conceived for reducing the detection complexity. We demonstrated that the proposed JMIM system is capable of outperforming its individual domain based counterpart, striking more flexible trade-offs between the BER performance and throughput. The learning method constructed is capable of approaching the performance of the maximum likelihood detector at a significantly reduced complexity. Furthermore, we showed that adaptive modulation can be applied for the selection of the JMIM DM design. We demonstrated that the CS-JMIM can flexibly adjust the transmission mode for accommodating time-variant channel conditions. We presented both KNN and DNN based adaptive schemes. Our simulation results showed that both the KNN and DNN-based approaches outperform the conventional threshold-based adaptive modulation. We also demonstrated that the DNN based adaptive design has a lower computational complexity and higher throughput than the KNN based approach.

REFERENCES

- [1] Y. Chau and S.-H. Yu, "Space modulation on wireless fading channels," in *IEEE 54th Vehicular Technology Conference. VTC Fall 2001. Proceedings (Cat. No.01CH37211)*, vol. 3, 2001, pp. 1668–1671 vol.3.
- [2] N. Ishikawa, S. Sugiura, and L. Hanzo, "50 years of permutation, spatial and index modulation: from classic RF to visible Light communications and data storage," *IEEE Communications Surveys Tutorials*, vol. 20, no. 3, pp. 1905–1938, 2018.
- [3] E. Björnson, E. G. Larsson, and T. L. Marzetta, "Massive MIMO: ten myths and one critical question," *IEEE Communications Magazine*, vol. 54, no. 2, pp. 114–123, 2016.
- [4] R. Y. Mesleh, H. Haas, S. Sinanovic, C. W. Ahn, and S. Yun, "Spatial modulation," *IEEE Transactions on Vehicular Technology*, vol. 57, no. 4, pp. 2228–2241, 2008.
- [5] E. Basar, "Index modulation techniques for 5G wireless networks," *IEEE Communications Magazine*, vol. 54, no. 7, pp. 168–175, 7 2016.
- [6] I. A. Hemadeh, M. El-Hajjar, and L. Hanzo, "Hierarchical Multi-Functional Layered Spatial Modulation," *IEEE Access*, vol. 6, pp. 9492–9533, 2018.
- [7] R. Abu-alhiga and H. Haas, "Subcarrier-index modulation OFDM," *2009 IEEE 20th International Symposium on Personal, Indoor and Mobile Radio Communications*, pp. 177–181, 2009.
- [8] D. Tsonev, S. Sinanovic, and H. Haas, "Enhanced subcarrier index modulation (SIM) OFDM," *2011 IEEE GLOBECOM Workshops (GC Wkshps)*, pp. 728–732, 2011.
- [9] E. Başar, Aygözü, E. Panayircı, and H. V. Poor, "Orthogonal frequency division multiplexing with index modulation," *IEEE Transactions on Signal Processing*, vol. 61, no. 22, pp. 5536–5549, 2013.
- [10] H. Zhang, L.-L. Yang, and L. Hanzo, "Compressed sensing improves the performance of subcarrier index-modulation-assisted OFDM," *IEEE Access*, vol. 4, pp. 7859–7873, 2016.
- [11] D. L. Donoho, "Compressed sensing," *IEEE Transactions on Information Theory*, vol. 52, no. 4, pp. 1289–1306, apr 2006.
- [12] L. Xiao, P. Yang, Y. Xiao, S. Fan, M. Di Renzo, W. Xiang, and S. Li, "Efficient compressive sensing detectors for generalized spatial modulation systems," *IEEE Transactions on Vehicular Technology*, vol. 66, no. 2, pp. 1284–1298, feb 2017.
- [13] T. Datta, H. S. Eshwariaiah, A. Chockalingam, and S. Member, "Generalized space-and-frequency index modulation," *IEEE Transactions on Vehicular Technology*, vol. 65, no. 7, pp. 4911–4924, 2016.
- [14] B. Chakrapani, T. L. Narasimhan, and A. Chockalingam, "Generalized space-frequency index modulation: Low-complexity encoding and detection," in *2015 IEEE Globecom Workshops (GC Wkshps)*, 2015, pp. 1–6.
- [15] R. Mesleh, S. S. Ikki, and H. M. Aggoune, "Quadrature spatial modulation," *IEEE Transactions on Vehicular Technology*, vol. 64, no. 6, pp. 2738–2742, 2015.
- [16] P. Patcharamaneepakorn, C.-X. Wang, Y. Fu, E.-H. M. Aggoune, M. M. Alwakeel, X. Tao, and X. Ge, "Quadrature space-frequency index modulation for energy-efficient 5G wireless communication systems," *IEEE Transactions on Communications*, vol. 66, no. 7, pp. 3050–3064, 2018.
- [17] Z. Li and J. Zheng, "Space-frequency shift keying in rapidly time-varying MIMO OFDM channels," in *2018 IEEE 87th Vehicular Technology Conference (VTC Spring)*, 2018, pp. 1–5.
- [18] C. Xu, P. Zhang, R. Rajashekar, N. Ishikawa, S. Sugiura, Z. Wang, and L. Hanzo, "'Near-perfect" ginite-cardinality generalized space-time shift keying," *IEEE Journal on Selected Areas in Communications*, vol. 37, no. 9, pp. 2146–2164, 2019.
- [19] S. Sugiura, S. Chen, and L. Hanzo, "Generalized space-time shift keying designed for flexible diversity-, multiplexing- and complexity-tradeoffs," *IEEE Transactions on Wireless Communications*, vol. 10, no. 4, pp. 1144–1153, 2011.
- [20] B. Shamasundar, S. Bhat, S. Jacob, and A. Chockalingam, "Multidimensional index modulation in wireless communications," *IEEE Access*, vol. 6, pp. 589–604, 2018.
- [21] S. Lu, I. A. Hemadeh, M. El-Hajjar, and L. Hanzo, "Compressed-sensing-aided space-time frequency index modulation," *IEEE Transactions on Vehicular Technology*, vol. 67, no. 7, pp. 6259–6271, 2018.
- [22] S. Lu, I. A. Hemadeh, M. El-hajjar, and L. Hanzo, "Compressed sensing-aided multi-dimensional index modulation," *IEEE Transactions on Communications*, vol. 67, no. 6, pp. 4074–4087, 2019.
- [23] S. Sugiura, S. Chen, and L. Hanzo, "Space-time shift keying: A unified mimo architecture," in *2010 IEEE Global Telecommunications Conference GLOBECOM 2010*, 2010, pp. 1–5.
- [24] J. Zheng and Q. Liu, "Low-complexity soft-decision detection of coded OFDM with index modulation," *IEEE Transactions on Vehicular Technology*, vol. 67, no. 8, pp. 7759–7763, aug 2018.
- [25] J. Liu and H. Lu, "Imnet: A learning based detector for index modulation aided mimo-ofdm systems," *2020 IEEE Wireless Communications and Networking Conference (WCNC)*, pp. 1–6, 2020.
- [26] S. Sugiura and L. Hanzo, "Effects of channel estimation on spatial modulation," *IEEE Signal Processing Letters*, vol. 19, no. 12, pp. 805–808, 2012.
- [27] Y. Acar, M. M. Leblebici, H. Doğan, and E. Panayircı, "Data detection based iterative channel estimation for coded SM-OFDM systems," in *2016 IEEE International Black Sea Conference on Communications and Networking (BlackSeaCom)*, 2016, pp. 1–4.
- [28] S. Katla, L. Xiang, Y. Zhang, M. El-Hajjar, A. A. M. Mourad, and L. Hanzo, "Deep learning assisted detection for index modulation aided mmwave systems," *IEEE Access*, vol. 8, pp. 202 738–202 754, 2020.

- [29] K. Satyanarayana, M. El-Hajjar, A. A. M. Mourad, P. Pietraski, and L. Hanzo, "Soft-decoding for multi-set space-time shift-keying mmWave systems: A deep learning approach," *IEEE Access*, vol. 8, pp. 49 584–49 595, 2020.
- [30] L. Xiang, Y. Liu, T. Van Luong, R. G. Maunder, L.-L. Yang, and L. Hanzo, "Deep-learning-aided joint channel estimation and data detection for spatial modulation," *IEEE Access*, vol. 8, pp. 191 910–191 919, 2020.
- [31] X. Cheng, M. Zhang, M. Wen, and L. Yang, "Index modulation for 5G: Striving to do more with less," *IEEE Wireless Communications*, vol. 25, no. 2, pp. 126–132, 2018.
- [32] S. Coleri, M. Ergen, A. Puri, and A. Bahai, "Channel estimation techniques based on pilot arrangement in OFDM systems," *IEEE Transactions on Broadcasting*, vol. 48, no. 3, pp. 223–229, 2002.
- [33] L. Lu, G. Y. Li, A. L. Swindlehurst, A. Ashikhmin, and R. Zhang, "An overview of massive MIMO: benefits and challenges," *IEEE Journal of Selected Topics in Signal Processing*, vol. 8, no. 5, pp. 742–758, 2014.
- [34] C. Xu, N. Ishikawa, R. Rajashekar, S. Sugiura, R. G. Maunder, Z. Wang, L.-L. Yang, and L. Hanzo, "Sixty years of coherent versus non-coherent tradeoffs and the road from 5G to wireless futures," *IEEE Access*, vol. 7, pp. 178 246–178 299, 2019.
- [35] L. Hanzo, J. P. Woodard, and P. Robertson, "Turbo decoding and detection for wireless applications," *Proceedings of the IEEE*, vol. 95, no. 6, pp. 1178–1200, 2007.
- [36] X. Feng, M. EL-Hajjar, C. Xu, and L. Hanzo, "Deep learning-based soft iterative-detection of channel-coded compressed sensing-aided multi-dimensional index modulation," *IEEE Transactions on Vehicular Technology*, pp. 1–16, 2023.
- [37] T. V. Luong, Y. Ko, N. A. Vien, D. H. N. Nguyen, and M. Matthaiou, "Deep learning-based detector for OFDM-IM," *IEEE Wireless Communications Letters*, vol. 8, no. 4, pp. 1159–1162, 2019.
- [38] T. Wang, F. Yang, J. Song, and Z. Han, "Deep convolutional neural network-based detector for index modulation," *IEEE Wireless Communications Letters*, vol. 9, no. 10, pp. 1705–1709, oct 2020.
- [39] M. Turhan, E. Öztürk, and H. A. Çırpan, "Deep convolutional learning-aided detector for generalized frequency division multiplexing with index modulation," in *2019 IEEE 30th Annual International Symposium on Personal, Indoor and Mobile Radio Communications (PIMRC)*, 2019, pp. 1–6.
- [40] P. Yang, Y. Xiao, M. Xiao, Y. L. Guan, S. Li, and W. Xiang, "Adaptive spatial modulation mimo based on machine learning," *IEEE Journal on Selected Areas in Communications*, vol. 37, no. 9, pp. 2117–2131, 2019.
- [41] H. Liu, S. Lu, M. El-Hajjar, and L.-L. Yang, "Machine learning assisted adaptive index modulation for mmWave communications," *IEEE Open Journal of the Communications Society*, vol. 1, pp. 1425–1441, 2020.
- [42] H. Liu, Y. Zhang, X. Zhang, M. El-Hajjar, and L.-L. Yang, "Deep learning assisted adaptive index modulation for mmWave communications With channel estimation," *IEEE Transactions on Vehicular Technology*, vol. 71, no. 9, pp. 9186–9201, 2022.
- [43] W. Koch and A. Baier, "Optimum and sub-optimum detection of coded data disturbed by time-varying intersymbol interference (applicable to digital mobile radio receivers)," in [*Proceedings*] *GLOBECOM '90: IEEE Global Telecommunications Conference and Exhibition*, 1990, pp. 1679–1684 vol.3.
- [44] H. V. Nguyen, C. Xu, S. X. Ng, and L. Hanzo, "Near-capacity wireless system design principles," *IEEE Communications Surveys Tutorials*, vol. 17, no. 4, pp. 1806–1833, 2015.
- [45] C. M. Bishop and N. M. Nasrabadi, *Pattern recognition and machine learning*. Springer, 2006, vol. 4, no. 4.
- [46] M. El-Hajjar and L. Hanzo, "EXIT charts for system design and analysis," *IEEE Communications Surveys and Tutorials*, vol. 16, no. 1, pp. 127–153, mar 2014.
- [47] S. Benedetto and G. Montorsi, "Serial concatenation of block and convolutional codes," *Electronics Letters*, vol. 32, no. 10, pp. 887–888, 1996.
- [48] I. Goodfellow, Y. Bengio, and A. Courville, *Deep learning*. MIT press, 2016.



Xinyu Feng received a BSc(Eng) degree with First Class Honours from University of Nottingham Ningbo, china and a BSc(Eng) in 2014. He obtained a MSc degree with distinction in wireless communication from the University of Southampton, UK in 2019. He is currently a PhD student at Next Generation Wireless Research Group under the supervision of Prof. L. Hanzo and Dr. M. El-Hajjar, University of Southampton, UK. His research interests include index modulation, Channel estimation and Detection and machine learning.



Mohammed El-Hajjar Mohammed El-Hajjar is an Associate Professor in the School of Electronics and Computer Science in the University of Southampton. He received his PhD in Wireless Communications from the University of Southampton, UK in 2008. Following the PhD, he joined Imagination Technologies as a design engineer, where he worked on designing and developing Imagination's multi-standard communications platform, which resulted in three patents. He is the recipient of several academic awards and has published a Wiley-IEEE book

and in excess of 140 journal and conference papers. His research is funded by the UK government and many industrial collaborators. Mohammed's research interests include the development of intelligent communications systems, energy-efficient transceiver design, MIMO, millimeter wave communications and Radio over fiber network design.



Chao Xu (S'09-M'14-SM'19) received a B.Eng. degree from Beijing University of Posts and Telecommunications, China, and a BSc(Eng) with First Class Honours from Queen Mary, University of London, UK, through a Sino-UK joint degree program in 2008, both in Telecommunications. He obtained a MSc degree with distinction in Radio Frequency Communication Systems and a Ph.D. degree in Wireless Communications from the University of Southampton, UK in 2009 and 2015, respectively. He is currently a senior research fellow working at

Next Generation Wireless Research Group, University of Southampton, UK. His research interests include index modulation, reconfigurable intelligent surfaces, noncoherent detection and turbo detection. He was awarded the Best M.Sc. Student in Broadband and Mobile Communication Networks by the IEEE Communications Society (United Kingdom and Republic of Ireland Chapter) in 2009. He also received 2012 Chinese Government Award for Outstanding Self-Financed Student Abroad and 2017 Dean's Award, Faculty of Physical Sciences and Engineering, the University of Southampton.



Lajos Hanzo (<http://www-mobile.ecs.soton.ac.uk>, https://en.wikipedia.org/wiki/Lajos_Hanzo) (FIEEE'04) received Honorary Doctorates from the Technical University of Budapest and Edinburgh University. He is a Foreign Member of the Hungarian Science-Academy, Fellow of the Royal Academy of Engineering (FREng), of the IET, of EURASIP and holds the IEEE Eric Sumner Technical Field Award.